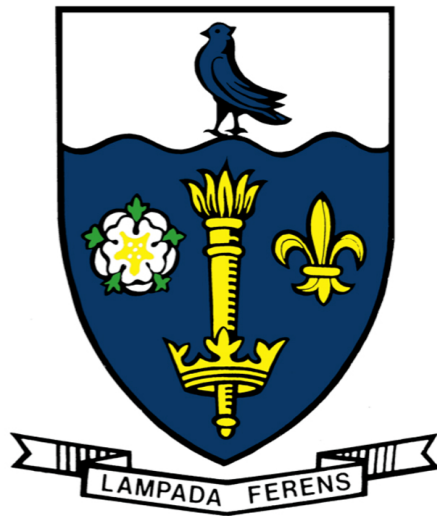


THE UNIVERSITY OF HULL



**THE EFFECTS OF GRAVITATION AND FLUID DYNAMICS ON
VELOCITY ESTIMATION BY STAGNATION POINT METHOD OF
A MINOR GALAXY CLUSTER MERGER, BY ANALYSIS OF FULL
HYDRO + N-BODY SIMULATIONS**

being a Thesis submitted for the Degree of Master of Science by Research
in the University of Hull

by

Thomas Marrick Fish, BSc (Hons)

June 2020

“The best way to observe a fish is to become a fish.”

– Jacques Yves Cousteau, Oceanographer, (*National Geographic*, 1952)

Acknowledgements

I would like to thank Dr. Elke Roediger for her kindness, patience and expertise; without her support I would not have been able to complete this thesis or had the opportunity to go to the Harvard-Smithsonian Center for Astrophysics (CfA) where a significant part of the work was undertaken. I thank Dr. Ralph Kraft and Dr. Yuanyuan Su for welcoming me to the CfA and providing me with a wonderful learning experience. Also, my thanks to all at the CfA, especially Gabriella Alvarez, John ZuHone, Paul Nulsen, William Forman and Christine Jones for enriching my time there.

My thanks also to Dr. Brad Gibson for leading such a friendly and excellent department, which I have been honoured to be a part of. From the galaxy cluster group, I'd like to particularly thank Dr. A. Sheardown and M. Hunt for their work and assistance, particularly at the beginning of my time in the group. I am also grateful to those who run VIPER, which was vital to this work.

This work would not have been possible without the funding by the Smithsonian Astrophysical Observatory during my student fellowship at CfA or the Department of Physics and Mathematics at the University of Hull for waiving my tuition fees.

Outside of astrophysics, I'd like to thank Maria Harkiolaki and the B24 team at Diamond for supporting my continued pursuit of this MSc. Finally, a big thank you to my friends and family; especially my partner, L. Ward, and my mum for supporting me.

Declaration of Originality

This thesis is submitted in partial fulfilment of the degree of Master of Science from the University of Hull. I declare that the work undertaken in this thesis is original and my own and was carried out under the supervision of Dr. Elke Roediger (University of Hull), Dr. Ralph Kraft (Harvard-Smithsonian Center for Astrophysics), and Prof. Brad Gibson (University of Hull). Where work, results, or ideas have been taken from other sources, those sources are explicitly referenced.

The nature of modern astrophysics is such that a number of co-authors is commonplace on research publications. Nonetheless, the work that has been or will be published from this thesis was the principle responsibility of myself in terms of driving the science case, analysis, and writing up. Some of the work and content of this thesis is from [Sheardown et al. \(2019\)](#), of which I was second author. These sections are: §3.3 and 4.2.3. All included text and figures from [Sheardown et al. \(2019\)](#) are by myself, with the exception of Figure 3.5, which has been cited appropriately. The one exception to this is in Appendix §7.1, which contains a derivation from Roediger et al. (in prep.), as this work informed the analysis in this thesis and therefore has been included with permission from E. Roediger.

Candidates signature: 

Date: 09/11/2020

Abstract

Galaxy clusters are collections of galaxies that grow by merging with galaxies or other clusters. Galaxy clusters are predominantly dark matter and a hot plasma called the intra-cluster medium (ICM), which can be observed through X-ray bright emission. Using X-ray observations of this fluid plasma, the stagnation point method (SPM) can be applied to estimate the velocity of a galaxy or subcluster merging with its host cluster. However, the efficacy of this cannot be tested in the real world due to the timescales over which mergers occur, so this thesis presents a careful analysis of a series of hydrodynamic + N-body simulations of the Fornax cluster to assess the applicability of several versions of the SPM. This analysis was applied throughout the simulations to cover a range of scenarios from a typical minor merger. A new modification to the SPM was also tested, which additionally considers the effects of gravity on the surrounding ICM. This modification improved the accuracy of the SPM during the first infall of each simulation, whereas the other methods significantly overestimated the velocity during this period. Following this, from pericentre passage until after apocentre passage, the SPM was found to be unsuitable as the flow could not be considered stable. During later infalls, the disturbed ICM made the definition of the free stream variables unreliable, which caused systematic issues and highlights the difficulties in defining free stream variables, even within a simplified, but realistic, scenario. This thesis sets out a range of recommendations to help assess validity and improve the application of the SPM to minor mergers. We also recommend the use of the new SPM that includes gravity, with careful modelling of the gravitational potential.

Contents

1	Introduction	1
1.1	Galaxy Clusters	1
1.1.1	The Intracluster Medium	2
1.1.2	Gravitational Potentials and the Existence of Dark Matter	4
1.2	Galaxy Cluster Mergers	5
1.2.1	Fornax & NGC 1404	8
1.3	Thesis Aims	10
2	Theory of the Stagnation Point Method	11
2.1	The Analogy of Gas Flow Past a Sphere	13
2.2	The Stagnation Point Method	14
2.3	Modelling The Stagnation Point	15
2.3.1	Incompressible Method, No Gravity	16
2.3.2	Method with Compressibility, No Gravity	17
2.3.3	3D Method with Compressibility	18
2.3.4	Considering Gravity: the Stolen Atmosphere Effect	18
2.3.5	The New Method: with Compressibility and Gravity	19
3	Simulation and Analysis Methods	21
3.1	The Fornax Simulations	21
3.2	Defining Variables in a Simulation	23
3.2.1	Mimicking Stagnation Point Method Observations	23
3.2.2	Important Locations	31
3.2.3	Inside the Stagnation Point	31
3.2.4	Testing the Gravitational Potential	32
3.3	Simulating Slingshot Tails	32

4	Results	36
4.1	Stagnation Point Models	36
4.1.1	The Gravitational Potential	36
4.1.2	Velocity and Pressure	38
4.1.3	Three Dimensional Models	42
4.1.4	Inside the Stagnation Point	42
4.2	ICM Flow	46
4.2.1	Stable Flow	46
4.2.2	Classifying Periods of Flow	46
4.2.3	Slingshot Tails	48
5	Discussion	53
5.1	Stagnation Point Methods	53
5.1.1	When the Stagnation Point Method Cannot Be Used	53
5.1.2	Including Gravity	57
5.1.3	Additional Sources of Uncertainty	58
5.1.4	Velocity of NGC 1404 Through Fornax	60
5.2	Misleading Slingshot Tails	63
5.2.1	Flow Patterns	63
5.3	Flow Relative to a Galaxy	65
5.3.1	Direct Line-of-Sight Velocity Observations	66
5.4	Observing the Stolen Atmosphere	68
6	Summary & Future Work	70
6.1	Stagnation Point Methods	70
6.2	Slingshot Tails	71
6.3	Future Work	71
7	Appendices	74
7.1	Defining The Stolen Atmosphere	74

Bibliography

List of Figures

1.1	Examples of major and minor mergers	6
1.2	X-ray mosaic of the Fornax Cluster with comparative image with the azimuthal average subtracted to highlight sloshing/cold fronts	9
2.1	Photographs of flow around spheres	12
2.2	Schematic diagram showing the flow regions upstream from an infalling galaxy or subcluster	15
2.3	Graph showing pressure ratio-Mach number relation according to models with/without compressibility	17
3.1	Electron density slices showing the evolution of the three Fornax simulations from Sheardown et al. (2018)	22
3.2	Diagram relating an idealised flow schematic to both simulated and observational images	24
3.3	Variable slices to show the stolen atmosphere and illustrate the stolen atmosphere compression and how the upstream galactic edge was found	26
3.4	Plots to illustrate the definition of the free stream variables	29
3.5	The evolution of two minor merger simulations as they form slingshot tails, from Sheardown et al. (2019)	35
4.1	Mass enclosed within spheres of increasing radius around NGC 1404's centre throughout the V0 and V2 simulations	37
4.2	Results of the stagnation point method analysis for simulation V0	40
4.3	Results of the stagnation point method analysis for simulation V2	41
4.4	Upstream pressure profile with 3D model fitting	43
4.5	Pressure variation inside the galactic boundary at the current time for the V0 and V2 simulations	45

4.6	The flow patterns in and around galaxy clusters with overrun slingshot tails . .	50
4.7	The flow patterns in and around galaxies with arc-shaped slingshot tails	52
5.1	Slices of pressure and approximate emission showing the manually defined free stream locations after pericentre passage of the V2 simulation	56
5.2	Graph showing the relation between pressure ratio and Mach number to compare our new stagnation point method with current methods	61
5.3	Flow plot from the V0 simulation at the current time	65
5.4	A map of velocity along the z-axis weighted by X-ray intensity of the V2 simulation at the current time	67
5.5	Temperature projection plots weighted to show observation-like values	68

List of Tables

3.1	Initial gravitational potential values of NGC 1404 in Sheardown et al. (2018)	
	simulations	21

1. Introduction

“WHAT A CLUSTER”

– Ben & Jerry’s Homemade Holdings Inc., *“What A Cluster” flavour ice cream tub (2011-2014)*

1.1 Galaxy Clusters

Over cosmic timescales, hierarchical structure has formed in the universe through gravitational attraction (Navarro et al., 1997; Prasad et al., 2018). Specifically, the structure is created by accretion and merger of galaxies, groups, subclusters, and, finally, galaxy clusters (Kravtsov & Borgani, 2012). These galaxy clusters are collections of hundreds to thousands of galaxies (Gunn & Gott, J. Richard, 1972; Gott & Rees, 1975). Galaxy clusters are the largest gravitationally bound and stable, i.e. virialised, structures in the universe, with cluster mergers being among the most energetic events in the universe (Schneider, 2006; Markevitch et al., 1999).

Galaxy clusters that do not show any significant signs of recent or ongoing merger are called ‘relaxed clusters’ (Markevitch & Vikhlinin, 2007); they have a characteristic structure based around their gravitational potential. Firstly, the centre of a relaxed cluster is much more densely populated with galaxies than the outskirts (Zwicky, 1937). These dense central regions are dominated by elliptical galaxies, due to frequent galaxy mergers during cluster formation, which strip away the looser bound matter in spiral arms, whereas the more sparsely populated outskirts typically contain more star-forming galaxies (Gunn & Gott, J. Richard, 1972; Nulsen, 1982). At the centre of a relaxed cluster sits the most massive and dense galaxy of the cluster and this is called the brightest cluster galaxy (BCG) (Schneider, 2006). As the growth of clusters is tumultuous and ongoing, it is unlikely that a perfectly undisturbed cluster exists. However, these idealised relaxed cluster characteristics can be used as a benchmark against which to compare and analyse the merger history of other clusters, as well as the physics of ongoing mergers (Roediger et al., 2012; Su et al., 2017c; Ascasibar & Markevitch,

2006).

1.1.1 The Intracluster Medium

Although galaxy clusters are composed of many galaxies containing many solar systems, stellar mass only accounts for $\sim 5\%$ of the total mass. A hot, diffuse near-primordial gas (largely hydrogen and helium, somewhat enriched with heavier elements) called the intracluster medium (ICM) accounts for $\sim 15\%$ of the total mass, and the remainder ($\sim 80\%$) is dark matter (Schneider, 2006; Sadat, 1997).

The existence of galaxy clustering has long been recognised but the discovery of the ICM was more recent. As astronomical observation improved, it became evident that there was more to galaxy clusters than could be seen by conventional telescopes. To account for the discrepancy between the observed mass and the mass required to gravitationally bind galaxies, it was theorised that a cluster consists “mainly of ionized hydrogen and that stars can contribute only a small fraction to its total mass” (Kahn & Waltjer, 1959), a prediction that was confirmed thanks to the UHURU satellite (Cavaliere et al., 1971; Forman et al., 1972). Since then, there have been several missions for the purpose of X-ray observation, notably Einstein, ROSAT, Chandra, XMM–Newton, and Suzaku. Most recently, the eROSITA mission was launched in 2019 to provide an all-sky X-ray survey. These mission have greatly increased our understanding of the ICM by providing increased spatial and spectral resolutions, data with a higher signal-to-noise ratio, and other technological advancements.

We now know from X-ray observations and modelling that the ICM is a hot, diffuse, fully-ionised plasma, consisting mainly of hydrogen and helium (primordial gas), visible in the X-ray spectrum primarily by thermal bremsstrahlung emission (Sarazin, 1986; Markevitch & Vikhlinin, 2007). This plasma induces large scale magnetic fields, and has a temperature-density gradient that increases towards the BCG until the central $\approx 100\text{kpc}$, where the temperature significantly drops due to cooling flows that are typically present in less morphologically disturbed clusters (Fabian, 1994, 2002; Schneider, 2006; Kahn & Waltjer, 1959; Bonafede et al., 2011; Giovannini et al., 2009; Pratt et al., 2009; ZuHone & Markevitch, 2009). Typical values are $T \sim 5\text{keV}$ and $n_e \sim 10^{-4}\text{cm}^{-3}$ (Schneider, 2006; Vikhlinin et al., 2006), where $n_e \approx n_p$ (the number density of electrons and protons respectively). A relaxed galaxy cluster will have

a spherically symmetrical ICM distribution. Deviations from this settled ICM distribution, in particular the existence of shocks and sloshing, are useful for determining a cluster's merger history, as well as, for example, magnetic fields and the transport coefficients of the ICM (Vikhlinin & Markevitch, 2002; Sarazin, 2008; Roediger et al., 2015a; Su et al., 2017c; Kraft et al., 2017, among others). Additionally, an ICM will have an increased metallicity where stellar-enriched galactic gas has mixed with it. This occurs through several mechanisms: supernovae, active galactic nuclei (AGN) (Prasad et al., 2018), galactic gas stripping and sloshing during mergers (Ricker & Sarazin, 2001; Zuhone, 2011; Sheardown et al., 2019).

As mentioned, the X-ray emissivity is primarily via thermal bremsstrahlung, which is typically calculated using classical mechanics with a non-relativistic correction factor, named the Gaunt factor, applied. This bremsstrahlung emission is described in equation 1.1, simplified from Nozawa et al. (1998, Eq. 33), where $\langle \epsilon(\omega) \rangle_{NR} d\omega$ is the time-averaged emissivity over a range of angular frequencies, ω , k is a combination of constants, and g_{NR} is the non-relativistic Gaunt factor. In Eq. 1.1, the emission is assumed to be from a fully ionised, quasi-neutral plasma of fixed effective atomic number, i.e. only the wavelength, density, and temperature vary.

$$\langle \epsilon(\omega) \rangle_{NR} d\omega = k \cdot g_{NR}(\omega) \cdot \exp\left(-\frac{\hbar\omega}{k_B T}\right) \cdot \rho^2 T^{1/2} d\omega \quad (1.1)$$

This assumes relativistic emissions from shocks and other high-energy events are negligible. This assumption is considered valid because relativistic emissions do not appear to be significant even in extreme cases such as the supernova remnant Cassiopeia A, which is observed to be dominated by thermal bremsstrahlung when observed by current telescopes (Vink & Jacco, 2008). There are further complications from processes including recombination and charge transfer (Kaastra et al., 2008), but these are beyond the scope of this thesis and are negligible for the aspects discussed here. From equation 1.1, it can be seen that the X-ray emissions are strongly tied to the plasma density with $\langle \epsilon \rangle \propto \rho^2 T^{1/2}$ for high temperatures like that of the ICM. The temperature is typically measured by fitting an emission model to the X-ray spectrum, for example by using the algorithm outlined in Vikhlinin (2006). Finally, assuming that the ICM acts as an ideal gas, a value for pressure can be extracted.

1.1.2 Gravitational Potentials and the Existence of Dark Matter

The ICM and stellar components comprise all of the visible mass but there is a further component that dwarfs both: dark matter. Unlike the ICM, dark matter is still an unknown entity, though we can now characterise many of its properties with a relatively small uncertainty thanks to the careful analysis of observations.

Fritz Zwicky is generally considered to have been the first to use the term “dark matter” (DM) to refer to missing matter in the universe in his analysis of galactic rotations within the Coma cluster (Zwicky, 1933) and of the orbits of the galaxies around the cluster centre (Zwicky, 1937). In both cases, the stable rotation velocities observed were faster than could be explained by the visible mass alone, and were also too consistent, regardless of radial distance from the centre of the galaxy or cluster, to make sense.

The discovery of the ICM did not explain all the missing matter, prompting further analysis that led to the first observational confirmation of dark matter by Rubin et al. (1980), through the analysis of galaxy velocity curves. Velocity curves, also known as rotation curves, plot the velocity of rotation of the galaxy around the galactic centre, known as the circular velocity, as a function of radial distance from the galactic centre. Stable orbits around a single body, such as the planets of our solar system around the sun, are slower at increased distances from the cluster, but galaxy rotations don’t follow this scheme. Rubin et al. (1980) found that galaxies all had the expected central pattern of steep velocity increase within the core of the galaxy but, rather than the expected drop-off beyond this, the velocity curve flattens out at higher radii, implying much more mass distributed throughout the galaxy than can be explained by the visible matter.

The circular velocity is simply $v_{\text{circ}} = \sqrt{-\phi(r)}$ where ϕ is the gravitational potential that varies with r , the radial distance from the galactic centre. A typical galaxy has a $v_{\text{circ}} \sim 200 - 300\text{km/s}$ (Pizzella et al., 2005). Given the flat circular velocity value beyond the central gradient of velocity curves, it is clear that the gravitational potential cannot be described using a point mass model or a mass profile that follows the visible matter, so models have been developed to describe the visible and DM distributions. Currently the leading descriptions are the Hernquist & Lars (1990) and Navarro et al. (1995) (NFW) models, which

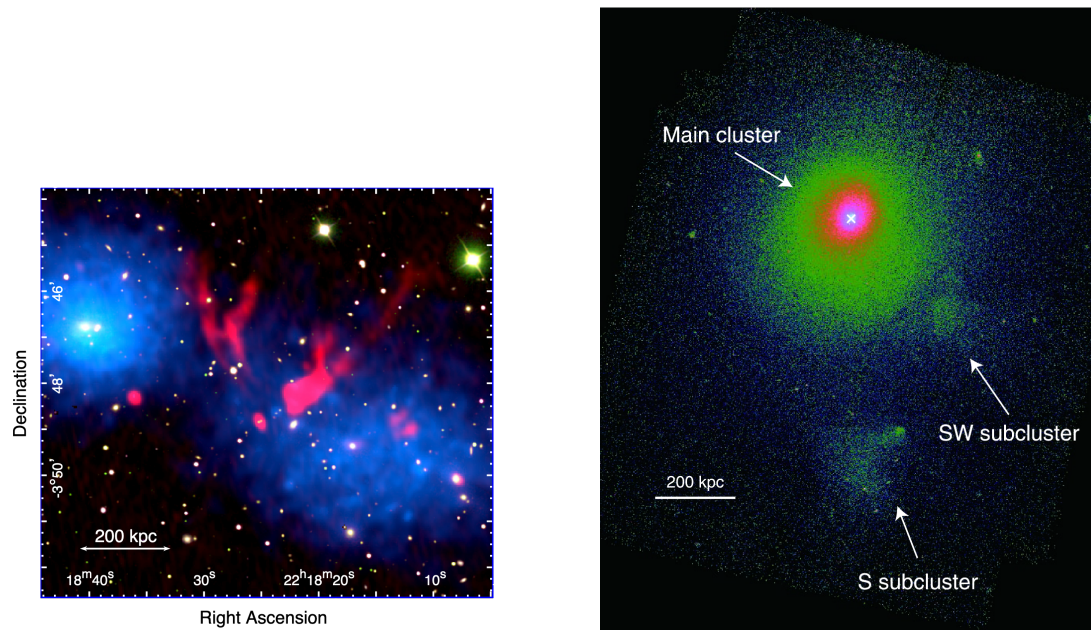
both provide a very close agreement with rotation curves and other observational data when paired with cold dark matter (CDM) halo profiles (Navarro et al., 1997; Avila-Reese et al., 1999; Jang-Condell & Hernquist, 2001).

The initial DM models have undergone further verification and refinement through analysis of cluster structure (Jones et al., 1979; Kravtsov & Borgani, 2012), measurements of gravitational lensing (Primack, 2009; Takizawa et al., 2010), most famously of the Bullet Cluster (Clowe et al., 2006; Markevitch et al., 2002; Milosavljević et al., 2007; Farrar & Rosen, 2007; Springel & Farrar, 2007, to name a few), the cosmic microwave background with WMAP (Jarosik et al., 2011), and more. Λ CDM is now the prevailing cosmological model, consisting of both cold dark matter (CDM), a low energy DM model, and dark energy (Λ).

1.2 Galaxy Cluster Mergers

Galaxy clusters are an excellent testing ground for many aspects of high energy physics and cosmology. ICM properties and merger mechanics give us information about the formation of structure within the universe while providing a view of extreme physical situations to test our understanding of the fundamental physics of the universe. Galaxy cluster mergers the most energetic events in the universe. A merger is an event where two clusters, or a cluster and a galaxy, strongly gravitationally interact, disturbing each other's structure, before combining to form a larger cluster. The point in the orbital path where the two clusters or galaxies are closest without merging is referred to as the pericentre, and the period of time when they are closest is called pericentre passage. Conversely, apocentre is the furthest point a body (a galaxy or cluster) reaches before falling back towards the other body. The period when the body is travelling from apocentre to pericentre is called an infall, and there can be multiple infalls during a merger. The bodies have little friction in the typical sense and are instead slowed primarily through the gravitational effect of dynamical friction (Schneider, 2006), which therefore speeds up the rate of merging.

A major merger (see Figure 1.1a) is described as two clusters of roughly equivalent size merging (i.e. a roughly 1:1 mass ratio), whereas a minor merger (see Figure 1.1b) is a smaller



(a) Major merger of 1E2215 and 1E2216

(b) Minor merger in Abell 85

Figure 1.1: Major and minor merger examples: (a) is the major merger of 1E2215 and 1E2216, shown as a composite of an SDSS optical image with X-ray overlay from Chandra (blue), and radio emission from GMRT (red) (taken from [Gu et al., 2019](#)); this is just before the collision of the two clusters. (b) is a background-subtracted Chandra X-ray observation of a minor merger, showing two subclusters undergoing merger with Abell 85 (taken from [Ichinohe et al., 2015](#))

body, such as a galaxy or subcluster, merging with a larger body (a host cluster or group). In a minor merger, the smaller body is typically described as ‘infalling’ towards the gravitational centre of the larger body. This infalling motion of the smaller body into and through the larger body causes ram pressure stripping as the ICM at the upstream edge becomes compressed, resisting the infalling galaxy and gradually stripping away the smaller body’s gas in the process.

In a typical minor merger, the galaxy (or subcluster) will gain velocity as it falls through its host cluster towards the BCG and will either collide head-on or, if it has a sufficient impact parameter (Ricker, 1998), the galaxy will pass the BCG. Depending on the mass ratio of the mergers, the infalling galaxy can significantly gravitationally affect the BCG, causing motion relative to the centre of the cluster and therefore ICM sloshing.

Treating mergers as a predominantly hydrodynamic situation is useful to study these effects, since it allows the application of simple analytical models that enable conclusions to be drawn from data that is limited by signal-to-noise and resolution. Simplifying the physical situation by using hydrodynamic assumptions enables useful information to be extracted from observations. However, it is important that these assumptions are investigated for systematic errors and general applicability. Simulations of increasing complexity have provided, and continue to provide, an additional way to make predictions that test current theory and our understanding of mergers by predicting/matching observed features (e.g. Morandi et al., 2015; De Grandi et al., 2016) and testing a range of situations over spatial and temporal scales that cannot currently be observed. Specifically, turbulence, magnetic fields, and tail and shock propagation are of particular interest when simulating mergers (Cen et al., 2014; Tonnesen & Stone, 2014; Roediger et al., 2015a,b; Kraft et al., 2017; Steinhauser et al., 2016).

This thesis will focus on applying analytical models used observationally to simulations, in order to test the assumptions behind the models. Specifically, it will look at the estimation of infall velocity within a minor merger since it is important to have an accurate measurement of the velocity of a galaxy (or subcluster) relative to the host cluster in order to fully understand the merger mechanics.

Minor mergers are a common scenario with many observable examples: A3667 (Vikhlinin

& Markevitch, 2002), NGC 4876 and others in Coma (Godwin et al., 1983); LEDA 87445 in Hydra A (De Grandi et al., 2016); A520 (Markevitch et al., 2005); NGC 1404 (Jones et al., 1997); M49 and others in Virgo (Böhringer et al., 1994); to name a few. Galaxies merging with their host cluster or group have common characteristics, including an extended turbulent wake, truncated atmosphere, and a shock front if the infall velocity is greater than Mach 1 (Ruderman & Spiegel, 1971; Machacek et al., 2005b; Kravtsov & Borgani, 2012; Roediger et al., 2012; De Grandi et al., 2016). These common characteristics make it easier to apply simple hydrodynamic analogies. One such hydrodynamic analogy is used to estimate the infall velocity of a galaxy from the stagnation point pressure at its upstream edge. This method and its physics are explained in Chapter 2, and the validity of this method is the main focus of this thesis.

1.2.1 Fornax & NGC 1404

Before outlining the aims of this thesis, it is important to introduce the Fornax cluster, as the simulations used in this thesis mostly focus on this specific case. The Fornax Cluster is a relatively low mass, cool-core cluster at a distance of ~ 17.5 Mpc (Neill et al., 2014) from Earth and a redshift of ~ 0.004600 (Abell et al., 1989). Due to its close proximity to us, Fornax and its constituent galaxies have been observed many times by ROSAT, Chandra, XMM-Newton, and others. The two brightest and most central galaxies in Fornax are: NGC 1399 (the BCG), which sits in the middle of the Fornax potential well; and NGC 1404, the closest galaxy to NGC 1399, which is undergoing a merger with NGC 1399.

NGC 1404 is an elliptical galaxy showing clear signs of ram-pressure stripping (as explained below in §2.1) as it falls towards the elliptical BCG, NGC 1399 (Machacek et al., 2005a; Su et al., 2017b). As NGC 1404 is falling into its host cluster, Fornax, this is a minor merger.

Given the faintness of ICM X-ray emission, turbulence and sloshing features are difficult to observe. However, Figure 1.2 (from Su et al., 2017c) shows clear signs of significant historical movement of NGC 1399 within the cluster centre, evidenced by the discontinuities in the surrounding ICM. Based on images of this kind and the analysis of tailored simulations, NGC 1404 is believed to be on its second or third infall (Su et al., 2017b; Sheardown et al.,

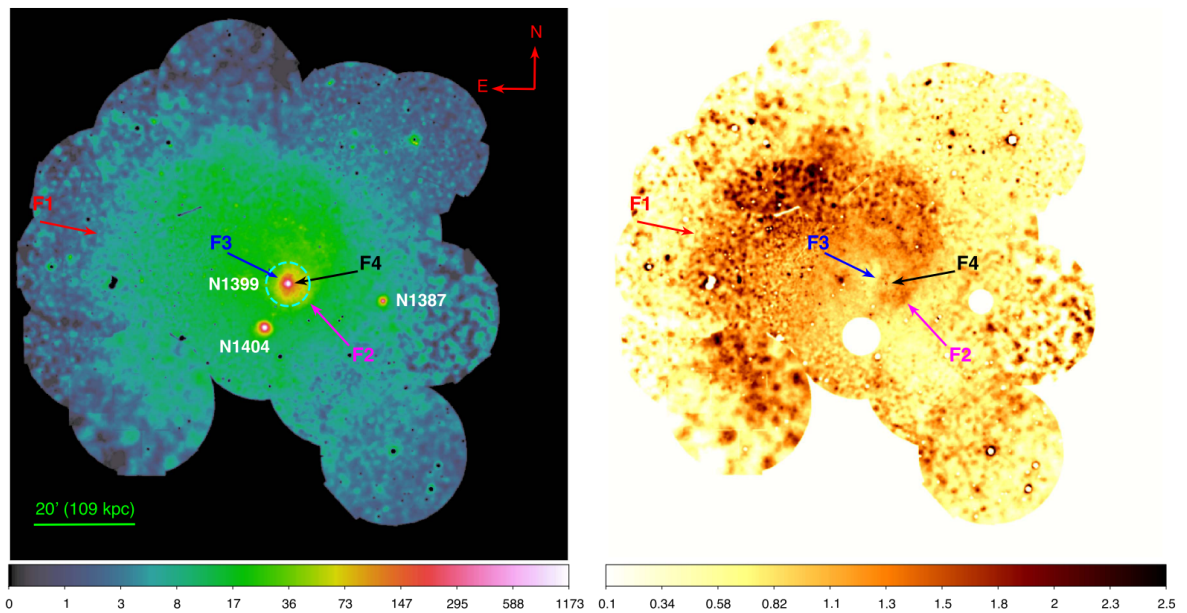


Figure 1.2: This figure was taken from [Su et al. \(2017c\)](#). The left image shows an XMM-Newton X-ray mosaic (0.5 to 2.0keV band) of the Fornax Cluster in the in units of cts/s/deg^2 . The image is exposure- and vignetting corrected- with instrumental backgrounds subtracted and point sources removed. On the right is a comparative image with the azimuthal average subtracted to highlight ICM sloshing/cold fronts. The lack of spherical symmetry shows significant evidence of ICM sloshing from previous infalls. The three most central galaxies, NGC 1399, NGC 1404 and NGC 1389, are labelled, along with the visible cold fronts (F1-4).

2018). X-ray observations show that NGC 1404 has a sharp density discontinuity along the ‘upstream’ edge (towards NGC 1399), a truncated atmosphere, and a visible tail/wake of stripped gas (Jones et al., 1997; Scharf et al., 2005; Su et al., 2017b), all of which are expected for a galaxy undergoing ram-pressure stripping in a stable flow (Roediger et al., 2015a).

The aforementioned features mean that NGC 1404 is a near-textbook example of a galaxy undergoing a minor merger with its host cluster, and is therefore a perfect case study for minor merger mechanics. Thanks to this and the excellent observational data available, the Fornax cluster centre offers a simple, data-rich scenario for analysis.

1.3 Thesis Aims

The main aim of this thesis is to validate the commonly used stagnation point method for estimating the velocity of a galaxy or subcluster within its host cluster. In Chapter 2, I describe the background physics and current versions of this method. These current versions all neglect the impact of the galaxy’s gravity, so in §2.3.4 I also show that gravity could play an important role. In §2.3.5 I describe a new variant of this method, and predict a new, potentially observable effect of the galaxy’s gravity: the ‘stolen atmosphere’.

I will validate the variants of the stagnation point method against hydrodynamical simulations, determining systematic uncertainties of the variants and identifying the periods of merger where no stagnation point method can be applied. A specific example of these periods – during the evolution of ‘slingshot tails’, a form of tail that emerges from unstable flow – will be given a particular focus through analysis of the flow in §4.2.3 and §5.2. Chapter 3 describes the simulations and analysis methods used and Chapters 4 and 5 will contain the results and discussion respectively. The discussion will describe the applications of these results to cluster mergers and the limitations of this work. Guidelines will be set out to help identify merger periods where the stagnation point method can be applied, as well as recommendations for the definition of observational variables, in the hope that these factors will be considered in future analyses. Finally, in Chapter 6.3, this thesis will outline some predictions for future observations and highlight some areas that would benefit from further study.

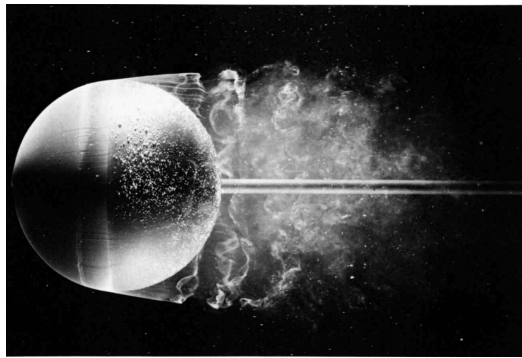
2. Theory of the Stagnation Point Method

In order to understand galaxy cluster mergers, the constituent parts need to be modelled. At the scale of galaxy clusters, both stellar components and DM can both be modelled using n-body simulations, whereas the ICM can be treated as a hydrodynamic fluid.

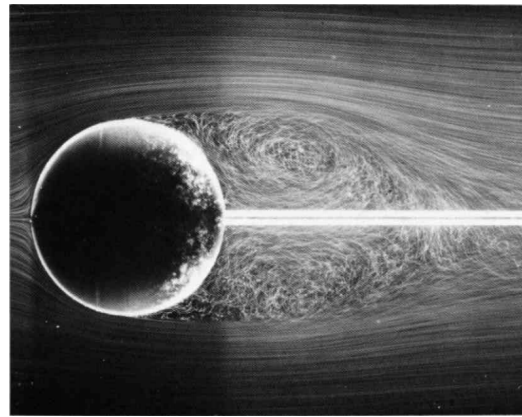
Hydrodynamics, in our case synonymous with fluid dynamics, is the theory that describes the motion of fluids. Much of hydrodynamics relies on certain assumptions, on the basis of which simple calculations can be used to describe otherwise complex situations. Such calculations include Bernoulli's incompressible flow equation, which is expanded upon below, and the Navier-Stokes equations, which describe viscous flow (Lifshitz & Landau, 1959). Hydrodynamics is therefore an invaluable tool for understanding and analysing the fluid motions of ICM.

For most studies, the ICM can be considered to be a very hot, diffuse, monoatomic gas (Milosavljević et al., 2007; Vikhlinin et al., 2001; Su et al., 2017b). Despite the fact that the movement of the ICM (an ionised plasma) induces magnetic fields, the ICM and cluster mergers are often treated as purely hydrodynamic scenarios because the magnetic pressure is much smaller than the thermal pressure, and the ICM can therefore be approximated as an ideal fluid at macroscopic scales (ZuHone & Roediger, 2016).

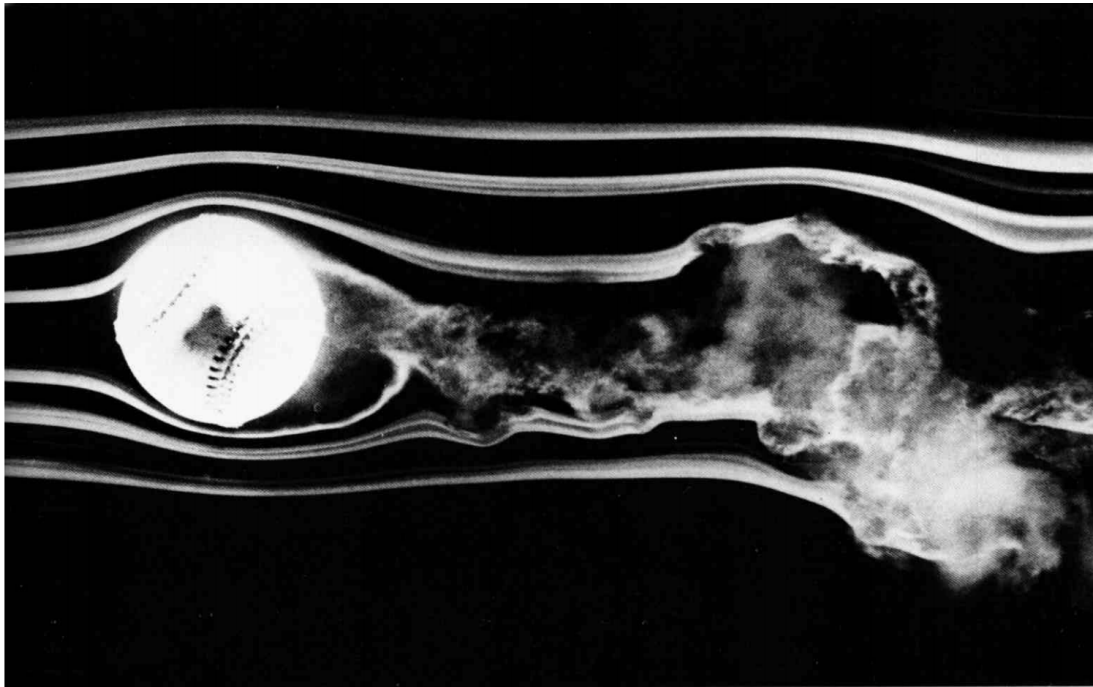
Thus far, the galactic atmosphere has not been discussed. The galactic atmosphere is the gravitationally bound gas within a galaxy, also known as the interstellar medium (ISM). In late-type galaxies the ISM is a complex, multiphase fluid due to the various heating and cooling processes within (Schneider, 2006). In contrast to this, in early-type (elliptical) galaxies, which have older stellar populations, the ISM is predominantly at about virial temperature, in the hot gas phase (Biermann & Kronberg, 1983; Su et al., 2015; Schneider, 2006). This is because ISM heating and cooling largely occurs through stellar activity, such as star formation and supernovae (Schneider, 2006; Tielens, 2005). For the purposes of this thesis we are considering the stagnation point method applied to elliptical galaxies, therefore it



(a)



(b)



(c)

Figure 2.1: Three photographs showing flow around spheres from [Van Dyke \(1982\)](#). (a) shows an instant as water strips a dye from a sphere; it is worth noting the separation of laminar flow just upstream of the equator. (b) shows a time-averaged image of air bubbles in water, illustrating the broader flow patterns around a sphere; the vortices downstream are emblematic of turbulent flow around a solid object (the size, shape, and positioning of the vortices are dependent on the geometry of the object). For both (a) and (b) the Reynolds number is $R = 1500$. (c) shows a baseball moving through smoke in a wind tunnel, illustrating how non-steady movement (the ball is rotating at 630rpm) can create asymmetry in the flow.

is reasonable to only consider the hot gas phase for simplicity. As such, we can say that for our case, the ISM has similar thermodynamic properties to the ICM. Following the terminology used in [Roediger et al. \(2015a\)](#), the hot gas in elliptical galaxies will be referred to as the galactic atmosphere, rather than ISM, to differentiate from the more complex ISM of late-type galaxies. To more generally talk about the fluid of the ICM and the galactic atmosphere, both will also be referred to as ‘gas’ for ease of description.

2.1 The Analogy of Gas Flow Past a Sphere

An infalling galaxy (or subcluster) can be summarised as a dense, gravitationally bound object falling through a hot, diffuse gas (ICM). The motion of the galaxy relative to the ICM causes ram pressure stripping, where the upstream pressure from the flow ‘ramming’ the galaxy pushes against the more loosely bound galactic atmosphere, and strips some of it in the process. This gives an infalling galaxy in a minor merger several general characteristics ([Roediger et al., 2015a](#)):

- The relative movement of the galaxy to the ICM pushes the galactic gas back, creating sharp density discontinuity at the upstream edge.
- The weakly bound gas at the sides of the galaxy is stripped through Kelvin-Helmholtz Instabilities (KHIs), forming a wake of stripped gas that mixes with the ICM.
- The downstream part of the galaxy’s atmosphere is not easily stripped and can be retained for a long time as a remnant tail.
- Toroidal vortices form downstream of the galaxy, trapping galactic matter in a dead-water region.

The flow patterns that cause these features can be seen in the model of a solid sphere or ellipsoid in a steady flow ([Roediger et al., 2015a](#); [Markevitch & Vikhlinin, 2007](#)) (see [Figure 2.1](#)).

For this analogy to be valid, the galactic atmosphere must persist. The galactic atmosphere is stripped when the ram pressure exceeds the internal gravitational pressure of the

galaxy (Mori & Burkert, 2000). From a more practical viewpoint, there are several parameters that decide the amount of gas that is stripped throughout a period of time, such as the merger mass-ratio (ratio of masses between the two merging bodies) and impact parameter (separation along the axis perpendicular to the velocity between bodies). If the mass-ratio of the merger is high and everything else kept equal, the atmosphere of the smaller body (the galaxy in our case) will be stripped faster than a low mass-ratio merger due to the denser ICM and faster infall increasing the ram pressure. However, it has been shown through simulation that even mergers with a high mass-ratio of 1:10 can survive beyond pericentre passage (unless it is a head-on collision, i.e. impact parameter of ≈ 0) (Zuhone, 2011; Sheardown et al., 2019), so this analogy is a useful one for a wide range of cases.

We can therefore draw useful analogies to the flow around a solid body (Roediger et al., 2015a; Lifshitz & Landau, 1959) to study flow around a stripped galaxy. In the next section, we will use this analogy to calculate the velocity of a galaxy moving through the ambient ICM from the ICM pressure at the upstream stagnation point.

2.2 The Stagnation Point Method

The stagnation point method is easiest to understand when considering the flow from the frame of reference at which the galaxy being measured is at rest. The stagnation point is the point at the upstream edge of a body where the flow velocity relative to the body is 0 (Lifshitz & Landau, 1959). This is the point where the flow splits around an object, which occurs in the middle of the upstream edge of the galaxy or sphere in the case of a steady flow (Batchelor, 2017). This causes a pressure enhancement relative to the ‘background’ pressure of the free-stream ICM, as the kinetic energy of the flow is converted to thermal energy (Lifshitz & Landau, 1959).

To provide a visual guide, the regions of flow have been defined in Figure 2.2. Additionally, all variables from the stagnation point will be given the subscript X_{stag} ; the region of compressed gas just ahead of the stagnation point will be referred to by X_{comp} ; and the free stream will be given the subscript X_{free} . In previous works these regions have been referred to as regions 0, 2, and 1 respectively.

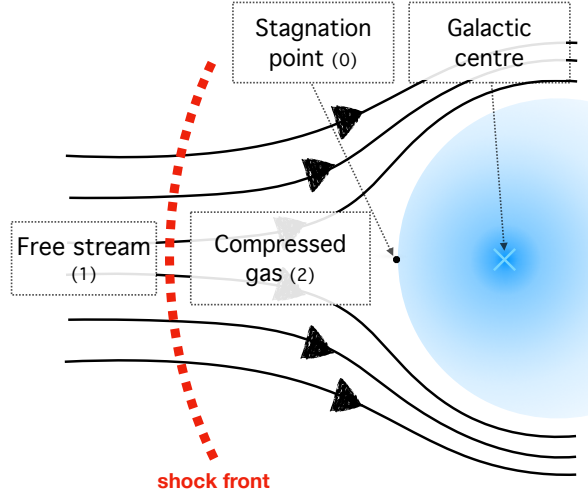


Figure 2.2: Schematic diagram showing the flow regions upstream from an infalling galaxy or subcluster. The different regions are: the free stream, assuming steady flow; the region of compressed gas just upstream of the galaxy (between the shock front and the galaxy when $\mathcal{M}_1 \geq 1$); and the stagnation point where the upstream flow velocity relative to the galaxy is 0 (referred to as 1, 2, 0 respectively in [Vikhlinin et al. \(2001\)](#); [Su et al. \(2017b\)](#)). In the literature there is a region 0' just inside the upstream edge that is treated as the stagnation point by observers due to data limitations.

We currently have two varieties of model, which will be explained in 2.3:

- A incompressible flow model in 2D (Eq. 2.4)
- A model that includes compressibility in 2D (Equations 2.5, 2.6), with a 3D expansion upon this by [Su et al. \(2017b\)](#)

2.3 Modelling The Stagnation Point

We consider a spherical galaxy with a sufficiently dense atmosphere in a steady flow of ambient ICM or gas. Assuming that galaxy's atmosphere is sufficiently dense that it is not fully stripped (i.e. bound to the galaxy with more gravitational force than is exerted by the ram pressure), it becomes an obstacle in the flow, similar to a solid sphere.

As a simple instructive case, we ignore the compressibility of the ICM (i.e. assume a constant flow density) and apply the incompressible Bernoulli equation ([Lifshitz & Landau, 1959](#)):

$$P + \frac{1}{2}\rho v^2 + \rho\Phi(r) = \text{constant (along a streamline)} \quad (2.1)$$

where P = pressure

ρ = density

v = velocity

$\Phi(r)$ = gravitational potential of the galaxy at distance r from its centre.

This equation expresses conservation of energy along a streamline. By assuming a spherical galaxy, we can use this equation to equate the free stream ICM and the stagnation point:

$$P_{\text{stag}} + \frac{1}{2}\rho v_{\text{stag}}^2 + \rho\Phi_{\text{stag}}(r) = P_{\text{free}} + \frac{1}{2}\rho v_{\text{free}}^2 + \rho\Phi_{\text{free}}(r) \quad (2.2)$$

By assuming the free stream region is far enough away from the galaxy that the gravitational potential is negligible (i.e. $\Phi_{\text{free}}(r) = 0$) and as $v_{\text{stag}} = 0$ by definition, we arrive at:

$$\frac{P_{\text{stag}}}{P_{\text{free}}} = 1 + \frac{P_{\text{ram}}}{P_{\text{free}}} + \frac{P_{\text{grav}}}{P_{\text{free}}} \quad (2.3)$$

$$\text{where } P_{\text{ram}} = \frac{1}{2}\rho v_{\text{free}}^2$$

$$P_{\text{grav}} = -\rho\Phi_{\text{stag}}(r)$$

P_{ram} is defined as the pressure contribution from the flow, which is known as the ‘ram pressure’, and P_{grav} as the pressure contribution from the gravitational potential interacting with the ICM. The stagnation point models used in this thesis are subsets and extensions of the above.

2.3.1 Incompressible Method, No Gravity

The most simple version treats the ICM as incompressible and ignores the effects of gravity by assuming $P_{\text{grav}} \ll P_{\text{ram}}$.

$$\frac{P_{\text{stag}}}{P_{\text{free}}} = 1 + \frac{P_{\text{ram}}}{P_{\text{free}}} \quad (2.4)$$

$$\text{where } P_{\text{ram}} = \frac{1}{2}\rho_{\text{free}}v_{\text{free}}^2$$

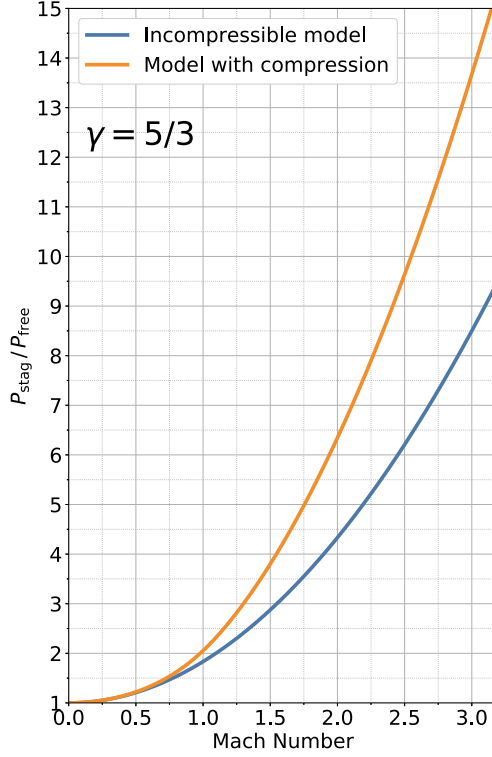


Figure 2.3: Plot comparing the $P_{\text{stag}}/P_{\text{free}}$ to Mach number relation of the stagnation point models with and without compressibility. As this plot shows the pressure ratio and the Mach number, it only depends on the thermodynamic degrees of freedom $\gamma = 5/3$ (note: $(\rho_{\text{free}} v_{\text{free}}^2)/P_{\text{free}} = \gamma \mathcal{M}_{\text{free}}^2$). The plot shows that, for a given $P_{\text{stag}}/P_{\text{free}}$, the incompressible model will estimate a significantly higher velocity than the model with compressibility. There is increasing disagreement at higher ratios of $P_{\text{stag}}/P_{\text{free}}$.

This allows us to calculate v_{free} from ρ and P_{stag} . However, if P_{grav} is significant this assumption will lead to an overestimated velocity.

2.3.2 Method with Compressibility, No Gravity

The ICM is not incompressible, so a different equation is needed to describe P_{ram} . One feature of fluid compressibility is that shocks form in trans/supersonic cases. [Vikhlinin et al. \(2001\)](#) applied equations from [Lifshitz & Landau \(1959\)](#) to incorporate compressibility, improving velocity estimation. By including compressibility but not gravity, we have:

If $\mathcal{M}_{\text{free}} \leq 1$:

$$\frac{P_{\text{stag}}}{P_{\text{free}}} = \left(1 + \frac{(\gamma - 1) \mathcal{M}_{\text{free}}^2}{2}\right)^{\frac{\gamma}{\gamma-1}} \quad (2.5)$$

If $\mathcal{M}_{\text{free}} > 1$:

$$\frac{P_{\text{stag}}}{P_{\text{free}}} = \left(\frac{\gamma - 1}{2}\right)^{\frac{\gamma+1}{\gamma-1}} \mathcal{M}_{\text{free}}^2 \left[\gamma - \frac{\gamma - 1}{2 \mathcal{M}_{\text{free}}^2}\right]^{\frac{-1}{\gamma-1}} \quad (2.6)$$

where $\mathcal{M}_{\text{free}} = v_{\text{free}}/c_s$

$\gamma =$ thermodynamic degrees of freedom.

Figure 2.3 shows that the compressible and incompressible methods differ significantly at Mach numbers of $\mathcal{M} \gtrsim 0.7$, with the compressible method predicting a lower velocity for a given $P_{\text{stag}}/P_{\text{free}}$.

2.3.3 3D Method with Compressibility

Both methods described above consider only the stagnation point, which is generally observationally inaccessible due to projection effects and its small physical size. Adding additional difficulty, the physical plane in which the merger is occurring is unlikely to be parallel with the plane of the sky. To allow for these factors, a 3D model was developed in Su et al. (2017b) using the assumption of spherical symmetry across the upstream edge. This model accounts for the angle α between the merger plane and the plane of the sky, and the angle θ from the stagnation point around the upstream edge (see Figure 3.2a). Both angles are measured relative to the centroid and defined by the upstream edge such that $P(\theta, \alpha = 0, 0) = P_{\text{stag}}$. This method also does not include gravity, based on the same assumption as for the other methods.

2.3.4 Considering Gravity: the Stolen Atmosphere Effect

In the past, P_{grav} has not been included as it is assumed to be negligible compared to P_{ram} (Markevitch et al., 2000; Vikhlinin & Markevitch, 2002; Markevitch & Vikhlinin, 2007; Kahn & Waltjer, 1959). Roediger et al. (in prep.) introduces the concept of the stolen atmosphere. The stolen atmosphere is the effect that a gravitating galaxy would have on a homogenous ICM if the galaxy suddenly appeared. Following this, it is reasonable to assume that the ICM will settle into hydrostatic equilibrium with the galaxy, causing an enhancement to the free stream variables (temperature, density, and therefore pressure) near to the galaxy as the ICM is pulled inwards by the galaxy's gravity and compressed. If we make the following assumptions:

- The ICM is an ideal gas
- The ICM will settle into hydrostatic equilibrium

- The settling is an adiabatic process

then Equation 2.7 can be derived (see Appendix §7.1 for the derivation):

$$\frac{P_{\text{grav}}(r)}{P_{\text{free}}} = \left(\frac{kT_{\text{free}} + \frac{2}{5}m_p \cdot (-\Phi(r))}{kT_{\text{free}}} \right)^{2.5} - 1 \quad (2.7)$$

where $r = r_{\text{strip}}$

In order to show the significance of the stolen atmosphere, we consider a stationary galaxy ($P_{\text{ram}} = 0$) with realistic parameters, where the stolen atmosphere pressure enhancement is misattributed to the ram pressure. By using the gravitational potential from the simulations, shown in Table 3.1, with a stripping radius of $\sim 8\text{kpc}$ and a $kT_{\text{free}} = 1.5\text{keV}$ for NGC 1404 (Machacek et al., 2005a) with Equation 2.7, a value of $P_{\text{grav}}/P_{\text{free}} = 3.2$ can be found. Plugging this into Equations 2.5/2.6, i.e. $P_{\text{stag}}/P_{\text{free}} = 1 + 3.2$, we get a Mach number of $\mathcal{M}_{\text{free}} = 1.59$. While the extent of overestimation will be smaller for any real example due to the non-linear relation between the pressure ratio and Mach number, it is clearly significant. To give a more realistic example, we used a Mach number of $\mathcal{M}_{\text{free}} = 1$, with the other values remaining the same, to calculate $P_{\text{stag}}/P_{\text{free}}$ from Equations 2.5/2.6, which equates to $1 + P_{\text{ram}}/P_{\text{free}}$. As the pressure ratios combine linearly, it is possible to add $P_{\text{grav}}/P_{\text{free}}$ to the previously calculated $1 + P_{\text{ram}}/P_{\text{free}}$ to get a new $P_{\text{stag}}/P_{\text{free}}$ value that includes gravity. Using the new $P_{\text{grav}}/P_{\text{free}}$ value with Equations 2.5/2.6 to solve for the Mach number returns a value of $\mathcal{M}_{\text{free}} = 1.80$: an overestimation of 0.8.

These two calculations show that the pressure enhancement at the stagnation point due to the galaxy's gravity, P_{grav} (equation 2.7) can be significant. Hence, whichever model for P_{ram} is used, P_{grav} should be included when describing P_{stag} , and therefore when calculating velocity.

2.3.5 The New Method: with Compressibility and Gravity

The best velocity estimates are currently given by equations 2.5/2.6 (or the equations from Su et al. (2017b) for 3D) for P_{ram} , and equation 2.7 for P_{grav} . Therefore, Equation 2.3 can be updated to use the improved equations for each pressure component:

$$\frac{P_{\text{stag}}}{P_{\text{free}}} = [\text{Eq. 2.5 or 2.6}] + [\text{Eq. 2.7}] \quad (2.8)$$

which expands to:

If $\mathcal{M}_{\text{free}} \leq 1$:

$$\frac{P_{\text{stag}}}{P_{\text{free}}} = \left(1 + \frac{(\gamma - 1) \mathcal{M}_{\text{free}}^2}{2}\right)^{\frac{\gamma}{\gamma-1}} + \left(\frac{kT_{\text{free}} + \frac{2}{5}m_p \cdot (-\Phi(r))}{kT_{\text{free}}}\right)^{2.5} - 1 \quad (2.9)$$

If $\mathcal{M}_{\text{free}} > 1$:

$$\frac{P_{\text{stag}}}{P_{\text{free}}} = \left(\frac{\gamma - 1}{2}\right)^{\frac{\gamma+1}{\gamma-1}} \mathcal{M}_{\text{free}}^2 \left[\gamma - \frac{\gamma - 1}{2 \mathcal{M}_{\text{free}}^2}\right]^{\frac{-1}{\gamma-1}} + \left(\frac{kT_{\text{free}} + \frac{2}{5}m_p \cdot (-\Phi(r))}{kT_{\text{free}}}\right)^{2.5} - 1 \quad (2.10)$$

This assumes that the stolen atmosphere is not affected by the motion of the body through the ICM, so this model may not work for high Mach number infalls where the body is moving through the ICM faster than the stolen atmosphere can be established by the ICM falling towards the body. Eq. 2.8 can also be extended to use the 3D model based on [Su et al. \(2017b\)](#) by calculating the gravitational potential at each point around the radius.

3. Simulation and Analysis Methods

“The ships hung in the sky in much the same way that bricks don’t.”

– Douglas Adams, *The Hitchhiker’s Guide to The Galaxy* (1979)

This thesis primarily relies upon the Fornax cluster tailored simulations from [Sheardown et al. \(2018\)](#), to which stagnation point analysis was applied. §3.1 will focus on the Fornax simulations, and §3.2 will focus on the definition of the different positions and variables needed for the stagnation point analysis.

However, there is an additional focus on ‘slingshot tails’. An understanding of these slingshot tails, a type of tail that forms due to unstable flow between pericentre and apocentre passage, is useful for the analysis of the stagnation point method as the unsteady flow during their evolution may invalidate the stagnation point method’s application. Slingshot tails and the simulations used for their analysis will be expanded upon in §4.2.3.

3.1 The Fornax Simulations

Initial Gravitational Potential of Simulated NGC 1404

$M_{\text{DM}} (M_{\odot} \times 10^{12})$	4.5
$a_{\text{DM}} (\text{kpc})$	45.0
$M_{\star} (M_{\odot} \times 10^{11})$	2.2
$a_{\star} (\text{kpc})$	1.5

Table 3.1: Initial double-Hernquist potential values used to set up NGC 1404 in [Sheardown et al. \(2018\)](#) simulations. Based on simple tests, we rely on the assumption that these values can accurately describe the potential of NGC 1404 at the stripping radius r_{strip} throughout the first two infalls.

This thesis presents an analysis of the stagnation point method by algorithmically applying observation-like methods to full hydrodynamic + N-body merger simulations of the Fornax-NGC 1404 merger from [Sheardown et al. \(2018\)](#) (shown in Figure 3.1). In these simulations,

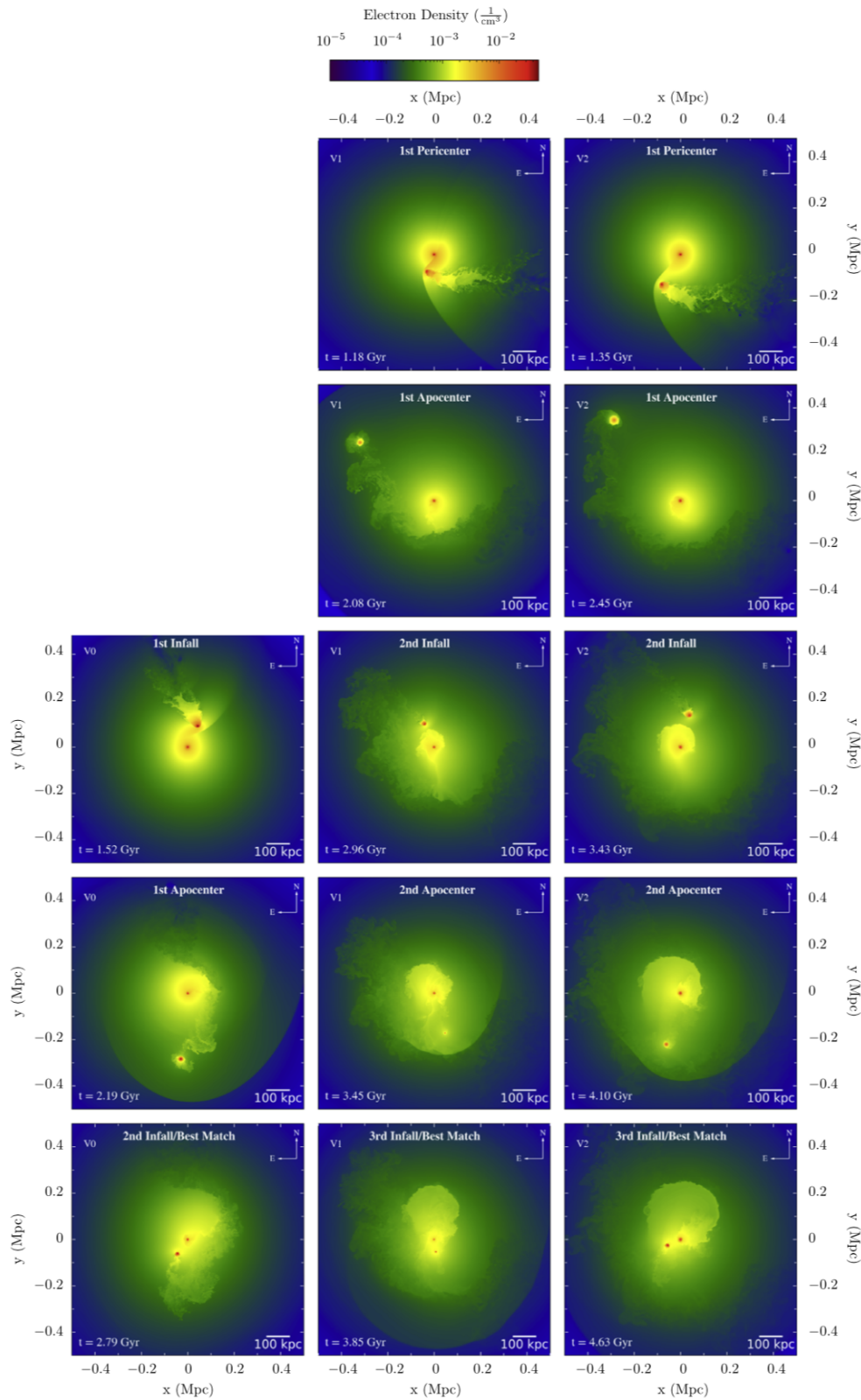


Figure 3.1: Electron density slices showing the evolution of the three Fornax simulations from Sheardown et al. (2018). Each column is a different simulation, left to right: V0, V1, V2. Each row has been matched to be at approximately the same development stage in the merger, such that the first infall of V0 best matches the second infalls of V1 and V2.

the N-body particles describe the non-collisional matter (DM and stellar), while the hydrodynamics describe the ICM and galactic atmospheres. In the simulations, Fornax and NGC 1404 were set up with double-Hernquist potentials (Hernquist & Lars, 1990) (Eq. 3.1 with values from Table 3.1) and atmospheres in hydrostatic equilibrium, and were then allowed to merge. In the course of the merger, NGC 1404 is successively stripped of its atmosphere during its motion through the Fornax ICM, leaving a significant wake and causing sloshing in the Fornax centre. The simulations follow NGC 1404 to its second or third infall when the best match to current observations occurs, depending on the initial set up conditions.

$$\Phi(r) = -\left(\frac{GM_{\text{DM}}}{r + a_{\text{DM}}} + \frac{GM_{\star}}{r + a_{\star}}\right) \quad (3.1)$$

As the easiest test case, we first analyse simulation V0 from Sheardown et al. (2018), in which NGC 1404 starts 650kpc from the Fornax centre with a tangential velocity of 150km/s. V0 provides a good compromise between giving a close match to observational data and maintaining simple dynamics with just two infalls (rather than the three of the other simulations). Simulations V1 and V2 were set up in the same way as V0 but with initial velocity $\mathcal{M} \approx 1$ and the same analysis was applied to each of them. Full details of these simulations can be found in Sheardown et al. (2018). This thesis will focus on V0 and V2 as they provide the best match to observations, while having different histories.

The yt module (Turk et al., 2011) was used to extract all the data that was taken directly from the simulations, including visualisations (slices and projections).

3.2 Defining Variables in a Simulation

Throughout our analysis, we will use the following definitions: Mach number $\mathcal{M} = v/c_s$; speed of sound in the medium $c_s = (\gamma \cdot P_{\text{free}}/\rho_{\text{free}})^{1/2}$; heat capacity ratio $\gamma = 5/3$, assuming a monoatomic gas.

3.2.1 Mimicking Stagnation Point Method Observations

To assess the accuracy of the different stagnation point methods, we need to determine the following quantities in a consistent manner at each time step in the simulations.

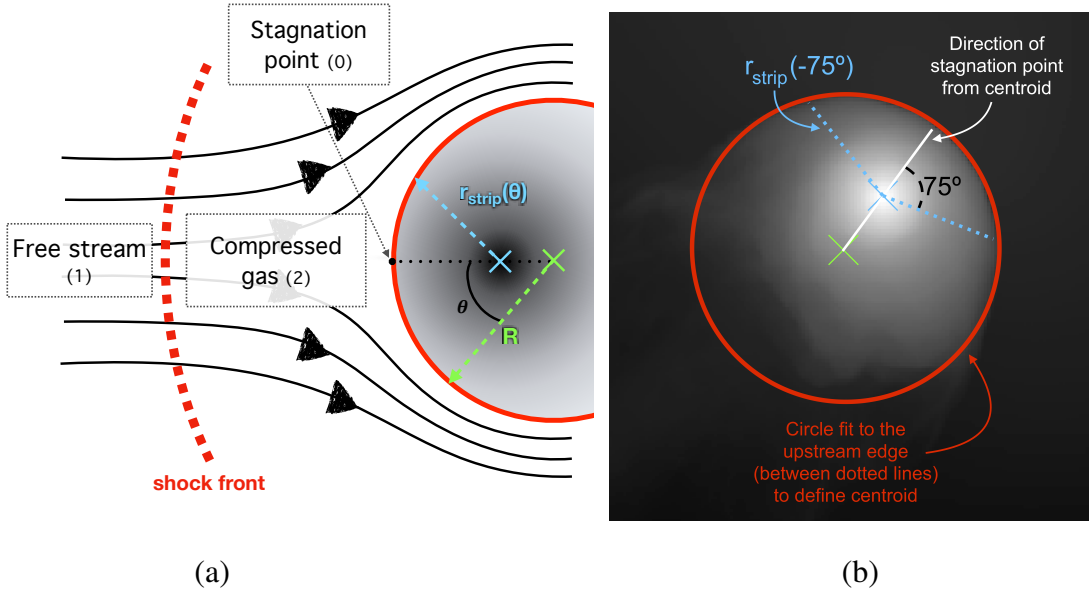


Figure 3.2: Diagram showing the upstream regions of an infalling galaxy or subcluster and comparing it to simulated and observational data.

(a) shows the different regions of flow schematically, as in Figure 2.2, as well as defining θ , R and $r_{\text{strip}}(\theta)$. R represents the radius from the centroid to the circle fitted to the upstream edge, θ is the angle around this circle from the stagnation point. The stripping radius r_{strip} varies with θ and is the distance to the galactic edge from the centre, as opposed to the centroid, as defined by the centre of mass.

(b) shows the centroid fitted to the upstream edge of the simulated galaxy (± 75 degrees from the stagnation point as shown by the blue dotted lines). This assumes, in line with Su et al. (2017b), that the upstream edge of the galaxy is spherically symmetric.

Position and Velocity

First, the orbital positions (centres) of NGC 1404 and Fornax were defined as the position of the highest density within their dark matter halos, found using the HOP method ([Eisenstein & Hut, 1997](#)). Then the average velocities of their respective dark matter halos, relative to the simulation grid, were used to define their velocities. From these velocities we set a second galactic velocity definition relative to the cluster, i.e. NGC 1404's velocity with respect to the Fornax centre. As the stagnation point method measures the velocity relative to the ambient ICM through which the galaxy is flowing, which will not be the same as either reference frame that could be defined, both velocity definitions will be shown. We did not further define the ambient ICM velocity as this quantity is currently inaccessible from observations. The most meaningful velocity to characterise as 'the infall velocity' is NGC 1404's velocity with respect to the Fornax cluster as a whole. However, a future study could also determine NGC 1404's velocity relative to the Fornax cluster's centre of mass as this moves within the overall cluster potential during the merger. For this reason, the velocity of NGC 1404 defined relative to the simulation grid is a good representative for NGC 1404's velocity with respect to the ambient ICM during the first infall. An additional consideration when defining the velocity, highlighted in [Zhang et al. \(2019\)](#), is how moving relative to a separate gravitational potential affects a galaxy's internal structure. Specifically, the distance between the galactic centre and the stagnation point changes due to the overall cluster potential. This change is evidenced in our simulations by the sloshing around NGC 1404's core. This means the upstream edge will be travelling at a different velocity to the galactic core when close to another gravitational potential. However, we have chosen not to use the location of the stagnation point to define velocity as the stagnation point is not in a fixed physical location on the upstream edge. In addition, the value difference between these velocity definitions will only be significant at pericentre, at which time the flow is no longer steady due to ICM gradients and the turning of the galaxy.

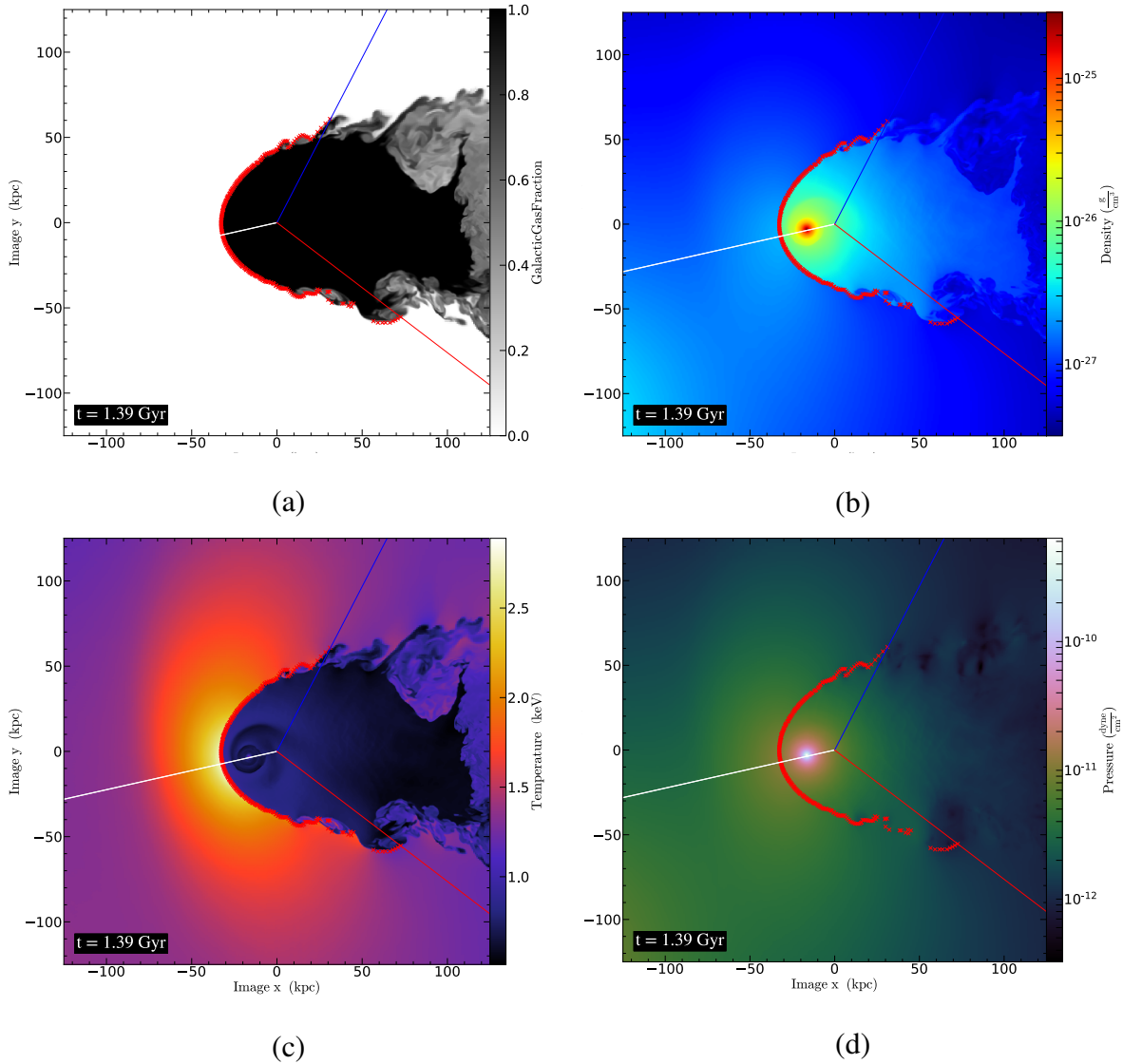


Figure 3.3: Slices through the merger axis of simulation V0 (Sheardown et al., 2018) at 1390Myrs to show the effectiveness of our edge-finding method and the distribution of variables relative to NGC 1404. These focus particularly on showing the enhancement to these variables centred around the gravitational potential (i.e. compression due to the stolen atmosphere effect). (a) shows the galactic gas fraction used to define the upstream galaxy edge; (b) shows the density; (c) shows the temperature; (d) shows the pressure. These images show that the density, temperature, and pressure are all enhanced over ambient ICM values at both the upstream edge and the sides of the galaxy. For all four images, the white line intersects the centroid and stagnation point, while the red and blue lines show the bounds of the galaxy edge-finding, and the red points show the locations where data is taken along the galactic boundary.

The Galactic Boundary

The stagnation point occurs where the ICM touches the upstream edge of the remaining NGC 1404 atmosphere. Thus, we need to define the edge between the NGC 1404 atmosphere and the Fornax ICM. To do this, we make use of the ‘galactic gas fraction’ parameter, a scalar quantity that is initially set to 1 for NGC 1404’s gas and 0 elsewhere. In order to have a consistent definition throughout all merger epochs, the following method was used: the galactic gas fraction was sampled along a line running from the centroid¹ in the direction of the galaxy’s velocity (as defined above), until the galactic gas fraction value dropped below 0.4; the first simulation cell beyond this threshold was defined as being on the upstream edge. This method was repeated at different angles, θ , from the velocity-centroid line, as shown in Figure 3.2, in order to define the entire upstream edge in the plane of the merger. A galactic gas fraction cutoff of 0.4 was chosen to avoid the detection of false edges due to the galaxy passing through previously stripped galactic gas during subsequent infalls. Figure 3.3 demonstrates the effectiveness of this method for finding the upstream edge.

Observationally, the stagnation point pressure is generally measured just inside the galactic boundary instead of at the actual stagnation point in the ICM due to the low signal-to-noise ratio of the ICM in X-ray data (Vikhlinin et al., 2001; Su et al., 2017b). This is justified because the gas just inside and outside of the upstream edge should be in pressure equilibrium. To limit the assumptions we are testing, we do not use this observational method of measuring the stagnation point, but measure the ICM properties as the real stagnation point.

The Stagnation Point

In an ideal steady flow scenario, the stagnation point would be in the middle of the upstream edge of the galaxy, in the direction of velocity from the galaxy’s centre. However, during a merger there is an ICM pressure gradient that increases towards the cluster centre, causing

¹This process was initially carried out from the galactic centre in order to find the upstream edge, which makes it possible to fit the centroid. This was then repeated from the centroid, as stated, so that all of the angles and points on the upstream edge are consistent (i.e. from the centroid, as shown in Figure 3.2). This will be explained further in a later section about defining the centroid.

asymmetry in the pressure distribution found along the upstream galaxy edge. In order to take this into account, we defined the location of the stagnation point using the maximum of a polyfit to the pressure profile along the upstream edge. The polyfit was applied to the data to remove small-scale fluctuations that occur due to instabilities (this will be shown in Figure 4.4).

The Centroid

In order to fit the 3D model, a centroid was necessary. Defining a centroid is a standard practice of observers (Su et al., 2017b,a; Vikhlinin et al., 2001; Machacek et al., 2005a) and is done by fitting a circle to the curve of the upstream edge of the galaxy. This is different to the galactic centre because the stripped atmosphere of the galaxy usually has a shorter upstream than downstream radius. For the purposes of algorithmically defining a centroid, a circle was fitted to the upstream galactic edge (as found using the galactic gas fraction, per §3.2.1) ± 75 degrees (from the galactic centre, see Figure 3.2b) from the stagnation point in the plane of the merger. The 3D stagnation point models were then fitted to the upstream edge pressure data points ± 60 degrees (defined by the centroid) from the stagnation point as they only apply to the upstream edge.

Free Stream Variables

The stagnation point methods rely on the assumption of steady flow, such that the free stream is far upstream where the body does not affect the gas properties. Measuring the free stream in clusters is difficult due to the ICM gradients (increasing pressure, temperature and density towards the cluster centre). In order to have a consistent method for all periods of flow, free stream values for ICM density, pressure and temperature were estimated by azimuthally averaging around the cluster centre, in the plane of the merger. This average was taken at a radius a_{Az} (Figure 3.4a) from the cluster centre set by the location of the closest edge of NGC 1404 with respect to the Fornax centre (using the NGC 1404 radius R from defining the centroid, solid-line circle in Figure 3.4d). During periods of unstable flow, radius R could not reliably be defined, so the radius a_{Az} was instead defined as the distance between the NGC

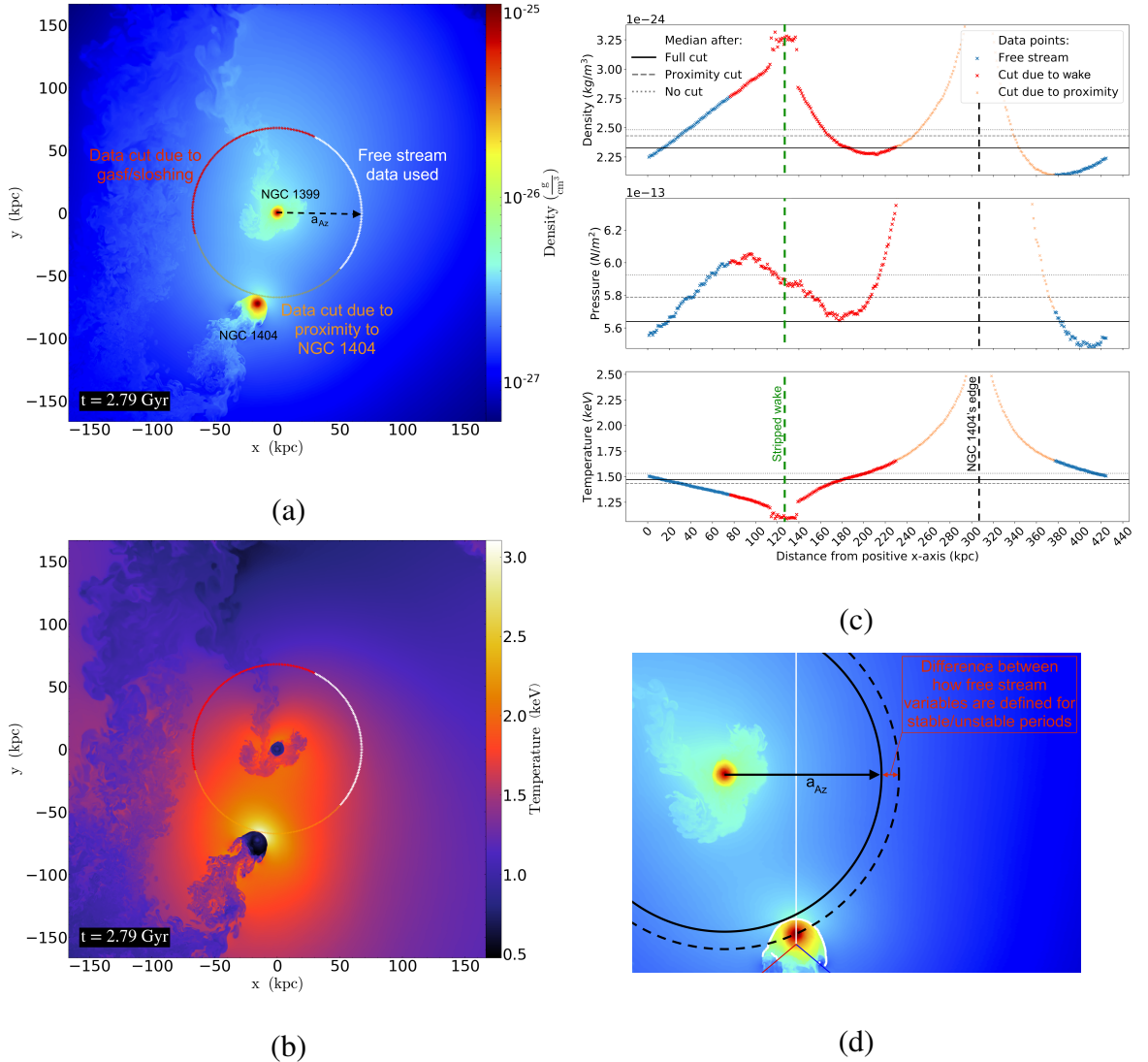


Figure 3.4: This figure shows how the free stream variables were defined throughout the simulation. These images are from the current time in simulation V0 (2790Myrs), to highlight the difficulty in defining these variables in a disturbed ICM. (a) shows the density slice in the plane of the merger, with the data points used to define the free stream variables labeled. (b) shows the temperature slice at the same time as (a), highlighting the large variation in temperature in the ICM and the existence of a channel of hotter gas between NGC 1404 and NGC 1399. (c) shows each of the azimuthal ICM profiles at the same time as (a) and (b), with the relative data cuts used to better define them and the averages the cuts resulted in. (d) illustrates the difference in how a_{Az} is defined for stable and unstable flow (the dashed-line circle is used during unstable periods, as the sphere fitted to the upstream edge, which also defines the centroid, cannot be fitted consistently during these periods).

1404 and cluster centres (dashed-line circle in Figure 3.4d). The changes in a_{AZ} definition can be seen in Figures 4.2 and 4.3 where discontinuities occur in the values calculated from free stream variables (including estimated velocity). The azimuthal average around the circle of radius a_{AZ} is not taken along the full circumference, but sections close to NGC 1404 or sections through its earlier wake were omitted. For the former, data points on the circumference within 65kpc of NGC 1404 were omitted. This value was chosen from visual inspection of azimuthal ICM profiles to avoid including ICM regions already affected by NGC 1404’s gravitational potential. For the latter, data points containing galactic gas were cut to avoid contamination by the galaxy’s wake. A physical representation of the cut regions can be seen in Figure 3.4a,b, and the effects of these cuts on the free stream variables are shown in Figure 3.4c. The final free stream variable values are the average of the remaining ‘good’ points - the median was used to avoid bias from any small disturbances that had not been cut.

The effects of these choices on the results are discussed Chapter 5.

Galactic Gravitational Potential

To take account of the stolen atmosphere effect, we used the initial potential of NGC 1404 throughout our analysis (Table 3.1, consistent between simulations); it was found through some simple tests (see §3.2.4) that mass lost due to tidal stripping is negligible, allowing us to use these values for all infalls.

The V2 simulation has an additional simulation field: gravitational potential energy. As this simulation field shows the gravitational potential energy due to all the mass in the simulation, not just NGC 1404, the values from this field cannot be used directly. Instead, the gravitational potential values for the stagnation point method were defined using the following assumption:

$$\Phi(r)_{\text{stag}} \approx \Phi(r)_{\text{stag,sim}} - \Phi(a)_{\text{ambient,sim}} \quad (3.2)$$

where $\Phi(r)_{\text{stag}}$ is the gravitational potential energy of NGC 1404 at the stagnation point, as specified in the stolen atmosphere equation (Equation 2.7), whereas $\Phi(r)_{\text{stag,sim}}$ is the total gravitational potential at the stagnation point of NGC 1404 from the simulation. $\Phi(a)_{\text{ambient,sim}}$

is the gravitational potential energy that is the average of two values taken along the relatively undisturbed z -axis at $\pm a$, the radial distance of NGC 1404's centre from the Fornax centre. This estimates the gravitational potential at the stagnation point if the gravitational potential of the Fornax cluster was taken away, although this doesn't account for the ICM asymmetries that develop during a merger, so will have significantly higher uncertainty during the later infalls.

Both gravitational potential definitions for the stagnation point will be shown in the final results from simulation V2.

3.2.2 Important Locations

For clarity, we emphasise that there are two equally important *centres*, and therefore radii, to consider in our analysis (shown in Figure 3.2):

- The galactic centre, as defined by the the peak of DM density, and the radial distance from this to the galactic edge, $r_{\text{strip}}(\theta)$.
- The centroid, as defined by the galactic boundary at the upstream edge, and the constant radial distance between this to the upstream edge, R . This is required to apply 3D models.

We calculate P_{grav} , the expected enhancement in local ICM pressure due to the galactic potential, using the radius between the galactic centre and upstream edge, $r_{\text{strip}}(\theta)$, whereas P_{ram} uses centroid radius R for the 3D model. Assuming the basic layout shown in Fig 3.2 during steady flow, the gravitational potential is closest to the upstream edge at the stagnation point so P_{grav} and P_{ram} will both be at a maximum at the stagnation point.

3.2.3 Inside the Stagnation Point

To investigate the effect of using X_{stag} as a proxy for the stagnation point, we compared the pressure inside the galactic boundary to the pressure at the upstream edge. To do this, the method used to identify the stagnation point pressure and pressure along the upstream edge was repeated at various points inside the galaxy. The resulting data has been plotted as a ratio

with the pressure at the same angle at the upstream edge, as defined by the centroid. This definition allows a close match to the distribution of data bins used as a proxy for the upstream edge pressure in [Su et al. \(2017b\)](#). The gas is expected to be increasingly compressed towards the galactic centre due to gravitational forces compressing the atmosphere, i.e. the stolen atmosphere effect.

3.2.4 Testing the Gravitational Potential

As a simple test, the mass within spheres of several radii centred around NGC 1404's galactic centre was measured at each time step. The radii used were 5kpc to 20kpc at 5kpc intervals, giving an insight into the evolution of the gravitational potential at the scale of the stripped gas atmosphere. Specifically, this test will show whether the amount of mass lost stripped from outskirts is significant enough to affect the gravitational potential at the stagnation point. While a significant amount of galactic gas is stripped throughout the simulation, it is expected that the DM-dominated gravitational potential will not significantly change throughout the simulation within 20kpc from the galactic centre, losing only loosely bound DM particles at larger radii.

3.3 Simulating Slingshot Tails

Slingshot tails occur in cases where two bodies pass each other at least once before colliding. In such cases it is important to look at the wider cluster to consider how the motions in the ICM affect the expected features, because turbulent gas motions and cold fronts are often formed ([Poole et al., 2006](#)). In a simple ram pressure stripping scenario, the head-tail morphology is simple, with the wake being pushed downstream and the sharpest density discontinuity in the middle of the upstream edge, as shown by [Acreman et al. \(2003\)](#); [Roediger et al. \(2015a\)](#). However, as [Roediger & Brüggén \(2006\)](#) showed, in the case of a merger where the infall angle is not directly towards the cluster centre, an asymmetry in the tail/wake is induced; the larger the angle, the greater the asymmetry. The tail direction is still considered when discerning the direction of motion, but the sharpest density discontinuity across the galactic edge is given more weight ([Machacek et al., 2005a](#); [Su et al., 2017b](#)). The position

of the longer tail/wake is assumed to trace the orbital path of the galaxy or subcluster as it merges with another body (Vijayaraghavan & Ricker, 2015). However, Sheardown et al. (2019) explains that this is not a safe assumption, citing real world examples and simulations from Poole et al. (2006); Zuhone (2011) as examples.

Sheardown et al. (2019) proposes a new form of tail, the slingshot tail, which arises shortly after pericentre passage. These slingshot tails are divided into two main modes: arc-shaped and overrun. Both modes of slingshot tail are produced by the asymmetry mentioned above, with the arc-shaped slingshot tail developing from a smoother, arching orbit than the overrun slingshot tail. In both cases the tail does not trace the previous orbital path, as might be expected.

Figure 3.5 (from Sheardown et al. (2019), Figure 2) shows the two simulations used for the slingshot tail analysis. The example of an overrun slingshot tail uses the V1 simulation from Sheardown et al. (2018), where NGC 1404 is the smaller body and NGC 1399 is the BCG of the Fornax cluster. The example of an arc-shaped tail is a simulation created for Sheardown et al. (2019). Both were created using FLASH (Fryxell et al., 2000) and are full N-body + hydrodynamic simulations.

As a part of Sheardown et al. (2019), I created several slices and projections of useful fields of the simulations (Figures 4 and 5 of the paper, or Figures 4.6 and 4.7 in this thesis), to show the mechanics behind the creation of each of these slingshot tail types. While I cannot claim sole credit for Section 5 of Sheardown et al. (2019) – the paper was produced through active discussion and collaboration within our group – I am primarily responsible for the analysis and writing in this section, and the aforementioned figures that are in it. An adapted version of this section can be found in §5.2.1. Figure 3.5 is A. Sheardown’s work from Sheardown et al. (2019). All other slingshot tails text in this thesis is original.

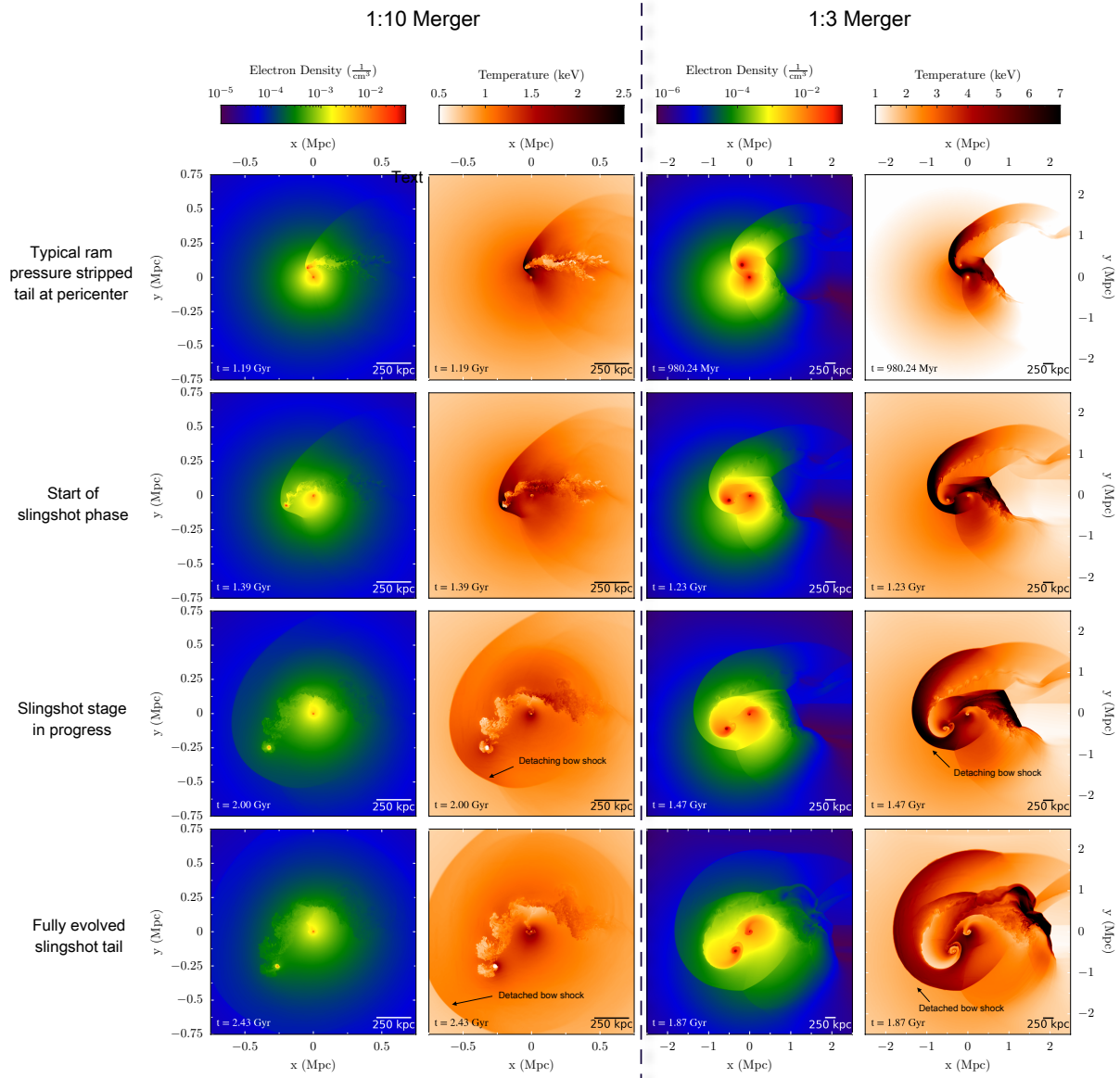


Figure 3.5: This figure and the following caption are by A. Sheardown and have been taken from [Sheardown et al. \(2019\)](#) to give context to work in this thesis that I contributed to [Sheardown et al. \(2019\)](#): Evolution of two different cluster mergers. The first and second column show electron density and temperature slices for a $\sim 1:10$ merger with a small impact parameter from the V1 simulation in [Sheardown et al. \(2018\)](#). The third and fourth column likewise show electron density and temperature slices but for a 1:3 merger we ran for this paper (following the simulation design of [Sheardown et al. \(2018\)](#)) using two idealized clusters with a pericenter distance of 330kpc. The first row shows the galaxy at pericenter with a typical ram pressure stripped tail. Note that in the 1:3 merger, the galaxy still contains a large amount of unstripped gas. The second row shows the start of the slingshot tail being produced as the galaxy slows toward apocenter. In the third row, for the 1:10 merger, the first phase of the overrun slingshot form is established, with the galaxy harboring an irregular shaped atmosphere as the remnant tail overruns directly the remnant atmosphere. For the 1:3 merger, the arc-shaped tail becomes a prominent feature. In the fourth row, for the 1:10 merger, the second phase is reached as the remnant tail continues to overrun the remnant atmosphere and fans out along the direction of apocenter away from the galaxy. For the 1:3 merger, the arc-shaped tail reaches its full prominence as the galaxy turns around and begins to infall again. In the fourth row, we also mark the bow shock that detaches from the slowing down galaxy. The detached bow shock will continue moving away from the cluster's center.

4. Results

“Salt, Salt, Salt, Salt, Salt, Salt...”

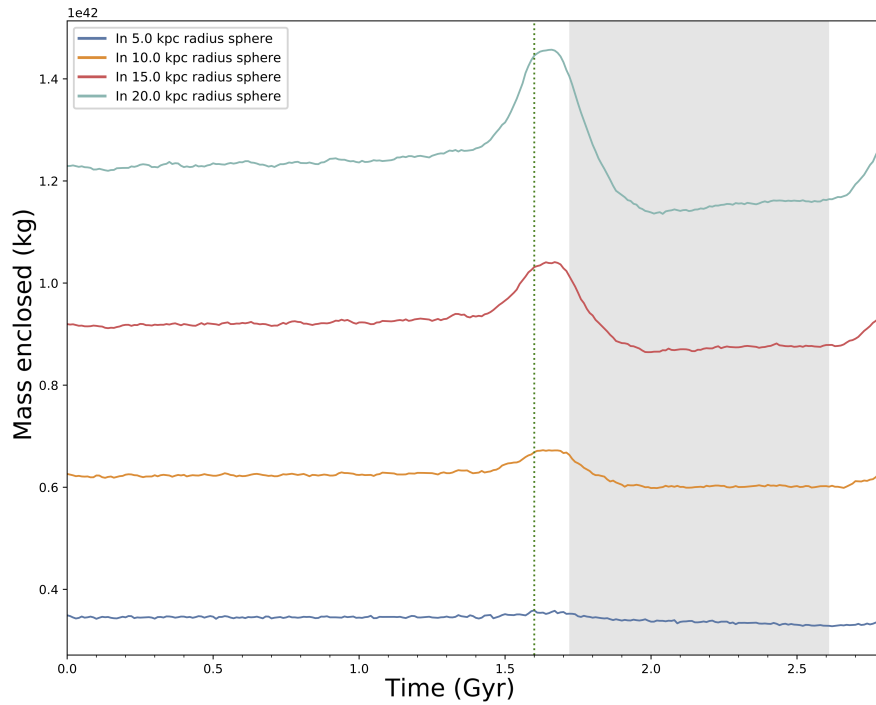
– Salt-N-Pepa, *Push It* (1987)

4.1 Stagnation Point Models

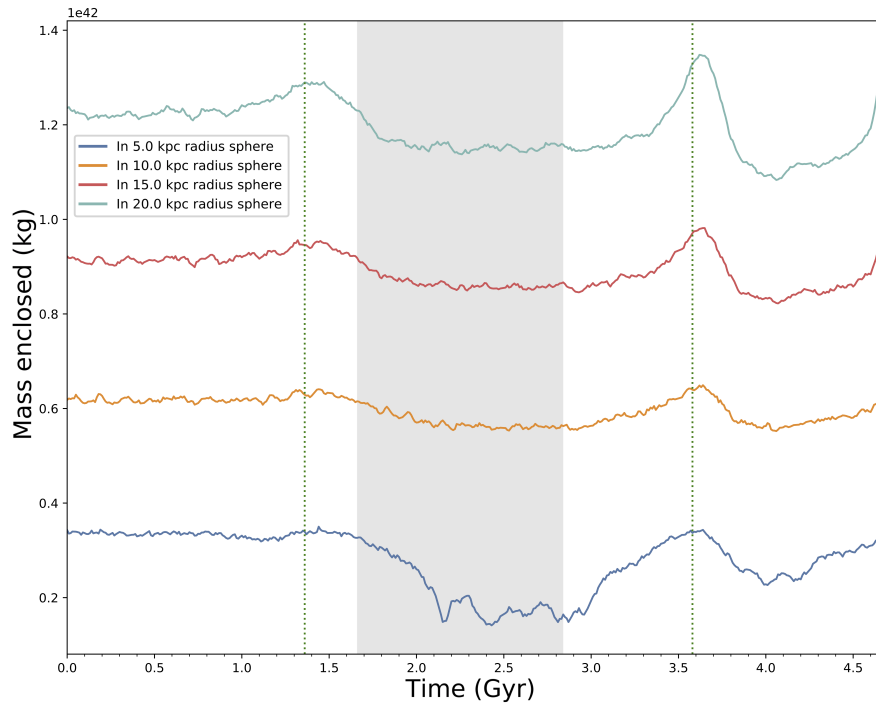
4.1.1 The Gravitational Potential

In order to confidently apply the stagnation point method that includes compressibility and gravity, the evolution of the gravitational potential of the galaxy had to be understood. The evolution of the galactic mass distribution was tested without taking account of morphology, by measuring the mass enclosed within spheres of increasing radius around the galaxy. The results of this are shown in Figure 4.1. The spheres show a peak in enclosed mass at pericentre passage, when mass from the cluster centre is within the outer spheres, and a slight loss ($\lesssim 5\%$) of mass after each pericentre passage. Additionally, the V2 simulation shows significant sloshing around the core after the first pericentre passage. This is evident from the fact that a significant amount of mass is ‘lost’ from the inner sphere, though this ‘loss’ is not reflected in the outer spheres. After pericentre passage, the galactic mass settles and the overall effect of this interaction can be seen. From this, it is clear that stripping (both of gas and, more significantly, DM particles) occurs predominantly at the outer regions, leaving the galactic core largely unchanged. While the core is generally stable, it is important to consider ICM sloshing when assessing the validity of the stolen atmosphere equation, as the change in mass distribution will affect the gravitational potential at the galactic edge, even if the overall mass within the galaxy has not changed significantly.

For simulation V0, there is no noticeable sloshing after the first pericentre passage, so it is probable that the effect of sloshing on the gravitational potential estimation will be insignificant for V0, though it is likely to affect V2. In fact, it can be seen in Figure 4.3 that the values of gravitational potential taken directly from the simulation significantly improved



Simulation V0



Simulation V2

Figure 4.1: The total mass (DM particles and gas) enclosed within spheres of increasing radius around NGC 1404's centre throughout the V0 and V2 simulations. There is no filtering for NGC 1404's mass, so larger spheres will include some ICM, and even the outskirts of NCG 1399 around pericentre passage. The pericentre passages (green dotted lines) and regions of instability (grey), as in Figures 4.2 and 4.3, have also been marked to give context.

the accuracy of the stagnation point method with compressibility and gravity, particularly after the first pericentre passage. However, the V2 results were additionally affected by intrinsic difficulty with defining the free stream variables after the first infall (to be discussed later). Due to these difficulties, it is safe to say that the gravitational potential is not the strongest source of uncertainty in the later infalls.

4.1.2 Velocity and Pressure

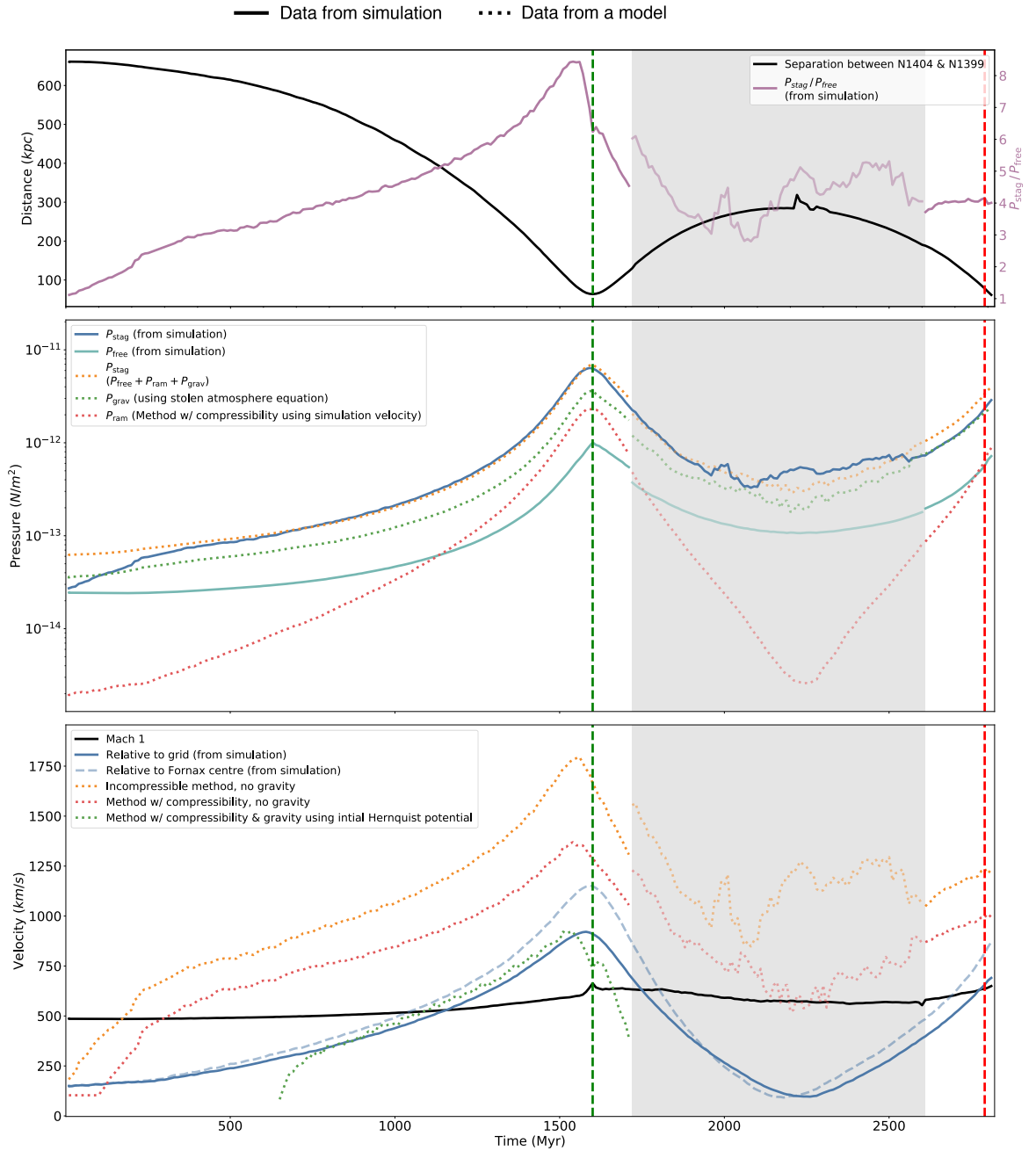
Figures 4.2 and 4.3 summarise the evolution of the merger by showing the variables from the stagnation point method analysis throughout the simulation. The main purpose of these figures is to compare NGC 1404's velocity, both relative to the simulation grid (solid blue line) and relative to the Fornax centre (dashed light blue line), with the estimates from the various stagnation point methods. In order to understand how the different pressure contributions affect the estimates, these figures also show P_{stag} , and all of its components according to our new model. Also plotted is the orbital separation between NGC 1404 and NGC 1399 (the Fornax centre) to help illustrate the progression of the merger.

On all of these plots, times and phases have been marked that are relevant to the periods described in §4.2.

This was repeated for simulation runs V0, V1, and V2 from Sheardown et al. (2018). Results for the slow infall V0 are in Figure 4.2. Figure 4.3 shows the result of the fast infall with larger impact parameter, V2. Results for simulation V1 (fast infall, low impact parameter) are very similar to the results from V2 and are therefore not reported here.

In Figure 4.3, some additional velocity estimates have been plotted, which were calculated using manually chosen free stream locations. These velocity estimates are for the period shortly after the first pericentre passage. This period was chosen to test whether these manually chosen free stream locations would correct systematic issues with the definition of the free stream variables particularly after pericentre passage. Following on from pericentre passage, as the galaxy approaches apocentre and turns back towards the BGC all methods are difficult to apply, and naive application causes a significant overestimation of velocity. For further analysis, see the discussion in Chapter 5.

In this specific scenario, $P_{\text{grav}} > P_{\text{ram}}$ for all epochs of the merger in all of the simulations,



Simulation V0

Figure 4.2: Plots showing the change in different variables over time for the first two infalls of V0:

The top plot shows the separation in kpc between the centres of NGC 1404 and Fornax to help illustrate the progression of the merger, as well as the $P_{\text{stag}}/P_{\text{free}}$ ratio to show how this important value varies throughout.

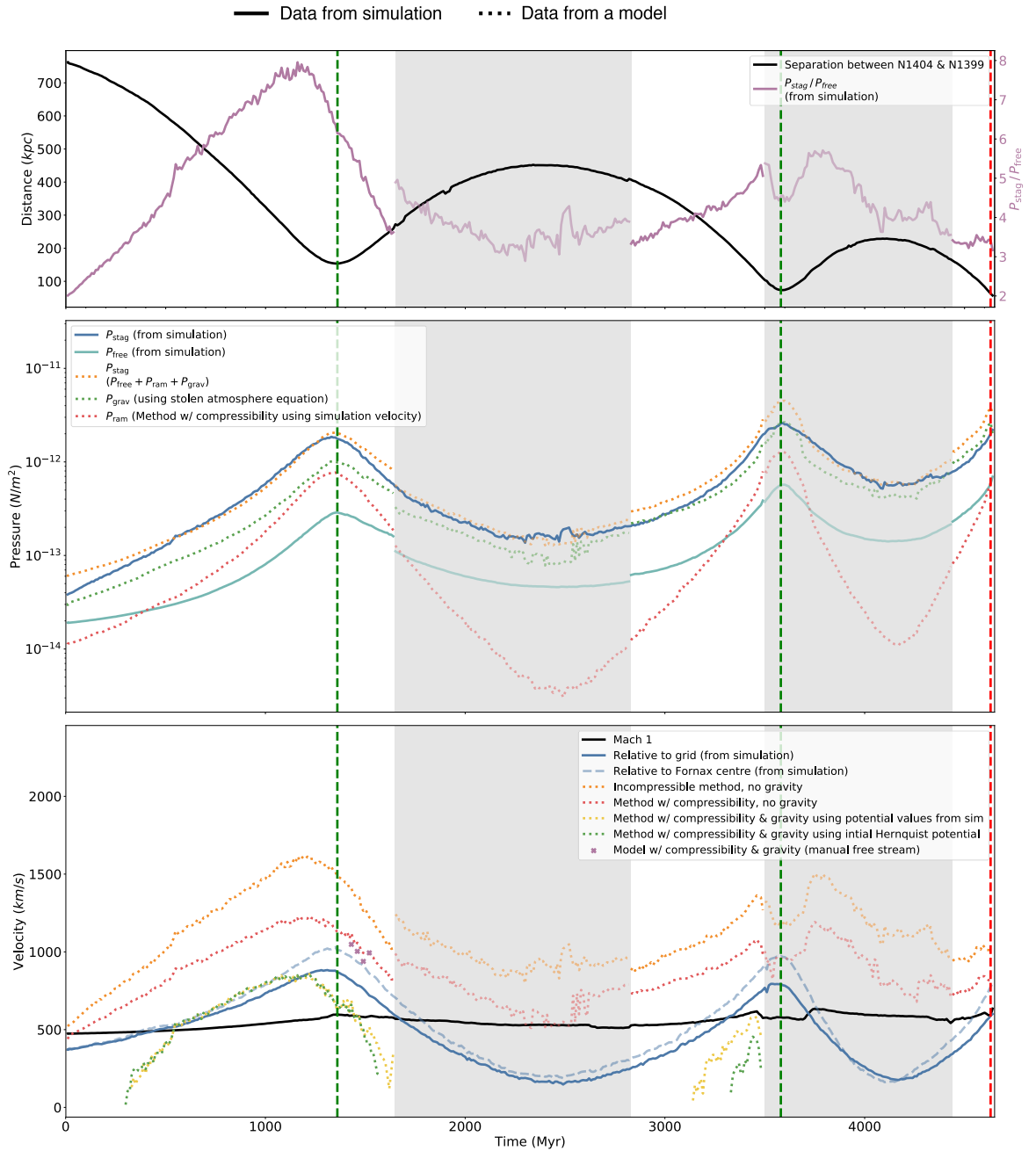
The middle plot shows the stagnation point pressure P_{stag} from the simulation in comparison to the P_{stag} from the new model (with compressibility and gravity), along with the component parts of P_{stag} . P_{ram} is calculated from NGC 1404's velocity relative to the grid using the 2D method with compressibility, no gravity; P_{grav} is from Equation 2.7 (Roediger et al., in prep.) and P_{free} is from the simulation as defined in §3.2.1.

Finally, the bottom plot shows the absolute speed of NGC 1404, with the velocity from the 2D stagnation point models over-plotted. 3D models have been omitted from this plot for clarity as the results were essentially the same but with small fitting errors. The blue solid line represents the velocity relative to the simulation rest frame (ICM starts off as stationary in this frame of reference), whereas the lighter dashed blue line shows the velocity of NGC 1404 relative to the Fornax centre. The black line shows the calculated velocity value of Mach 1 based on the free stream ICM.

This simulation shows the first two infalls of V0, up until the current time (the best match to observations). Centroid fitting issues only occurred during the unstable flow period and only for a short time as the galaxy was settling into regular flow patterns from the initial conditions, so are acceptable for our purposes.

indicating that pressure enhancement from the galaxy's gravity is more important than the enhancement from motion through the ICM. To use a specific example similar to the current observations, at 2780Myrs (near the current time) in the V0 simulation, we were able to calculate a ratio of $P_{\text{grav}}/P_{\text{ram}} = 2.5$. While the real Fornax cluster will be more complex than this simulation, this result highlights the importance of P_{grav} to P_{stag} . The value of P_{stag} calculated using our updated method (including compressibility and gravity) closely matches the true value from the simulation during the first infall of each simulation. In contrast, the previous best method (with compressibility, not gravity) is $\sim 60\%$ too high during the stable infall periods.

All estimates work best for the first infall when the ICM is still largely at rest. P_{grav} is overestimated during later infalls: $P_{\text{grav}} \approx P_{\text{stag}}$ during the second infall of V0, likely due to a combination of the mass stripped from NGC 1404 that isn't accounted for in the P_{grav} calculations and the sloshing within each galaxy and the ICM). However, this should not be significant enough to change the fact that P_{grav} is consistently larger than P_{ram} , even in the higher velocity simulation of V2, so the hypothesis that $P_{\text{grav}} > P_{\text{ram}}$ in these simulations is



Simulation V2

Figure 4.3: Plots showing the stagnation point analysis results for the first two infalls of V2 (as Figure 4.2 for V0 with a couple of additions). An additional line has been plotted to show the velocity estimate from the stagnation point method with compressibility and gravity, using the gravitational potential values taken directly from the simulation. Some additional points have also been plotted after the first pericentre — when the algorithmic methods have systematic problems — using manually chosen free stream locations and the new method (with compressibility and gravity). This plot shows two full infalls, with a higher initial velocity than V0.

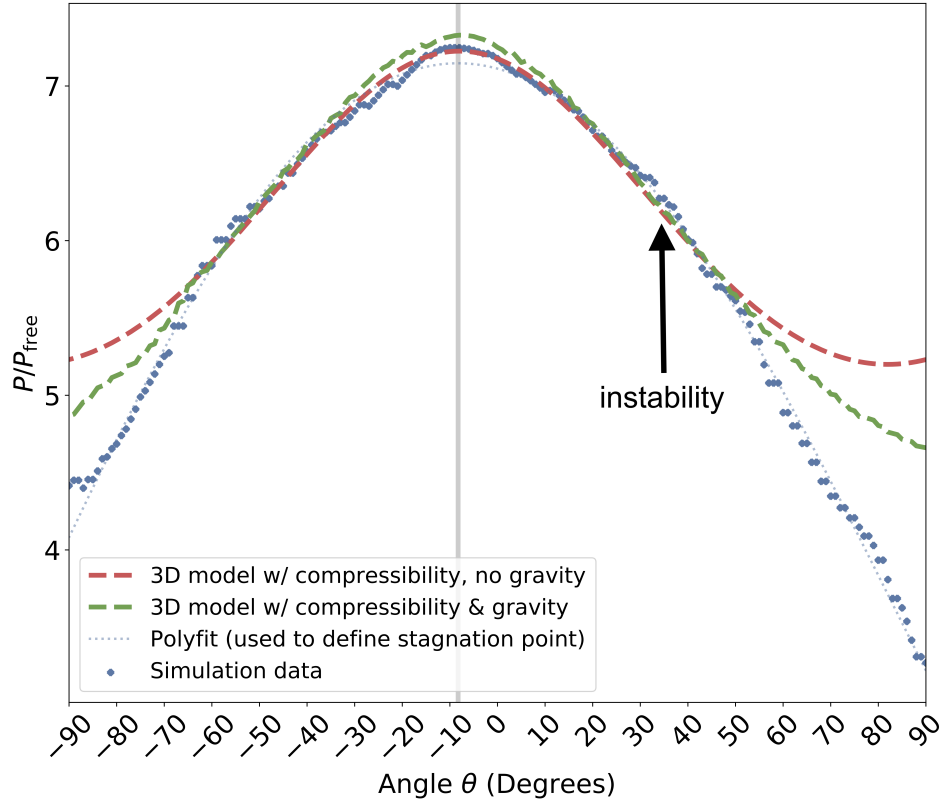
correct. The applicability of the stolen atmosphere effect to the stagnation point method will be discussed later.

4.1.3 Three Dimensional Models

Figure 4.4 shows pressure data at 980Myr, during the first infall of [Sheardown et al. \(2018\)](#)'s V2 simulation, along with the 3D model developed by [Su et al. \(2017b\)](#), both with and without gravity, fitted to that data. While the models fit the central region well, the model with gravity has a stagnation point pressure ratio that is higher than the data, which could be improved with careful weighting. This shows that this model fits the data for a wide range of angles from the stagnation point across the upstream edge. However, at approx. +30 degrees there is an instability that, depending on the angle of viewing, could cause significant errors. It is therefore clear that, while using the spherical assumption in the 3D model is a powerful tool to analyse mergers that are not in the plane of the sky, it is important to check carefully for signs of asymmetry. Additionally, this plot shows that adding the stolen atmosphere effect slightly improves the fit of the model to instabilities, while not accounting for the effects of instabilities on the flow (e.g. pockets of lower pressure in vortices). The velocity estimates that result from fitting the two 3D methods to the data are not an *exact* match to their 2D equivalents but were so close to them that it made the plots confusing, so we have not included them in Figures 4.2 and 4.3.

4.1.4 Inside the Stagnation Point

Observers typically use a proxy for the stagnation point, which is usually referred to as $0'$ ([Vikhlinin et al., 2001](#); [Su et al., 2017b](#)), but for consistency of naming style is called X_{stag} in this thesis. This proxy is used because of the size of the stagnation point and its location: the stagnation point is infinitesimally small, so is difficult to observe in terms of angular resolution and depth. To further complicate things, the stagnation point is well hidden by projection. The ICM in front and behind the stagnation point obscures its emission. Then, if the infall is not perfectly in the plane of the sky the emission from the galaxy will dwarf, and therefore hide, all other emission from the line-of-sight at the stagnation point. The second issue is the density of the stagnation point: as the ICM is very low-density, the signal is too

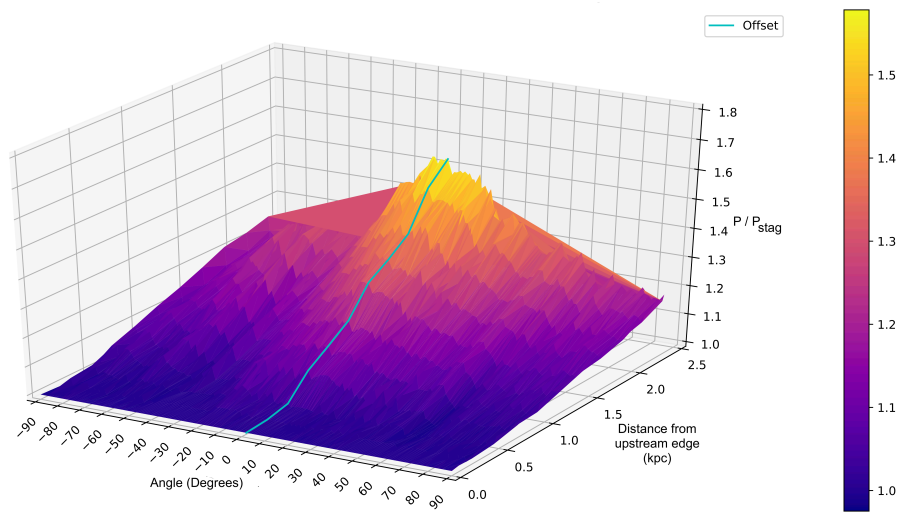


Simulation V2 at 980Myrs

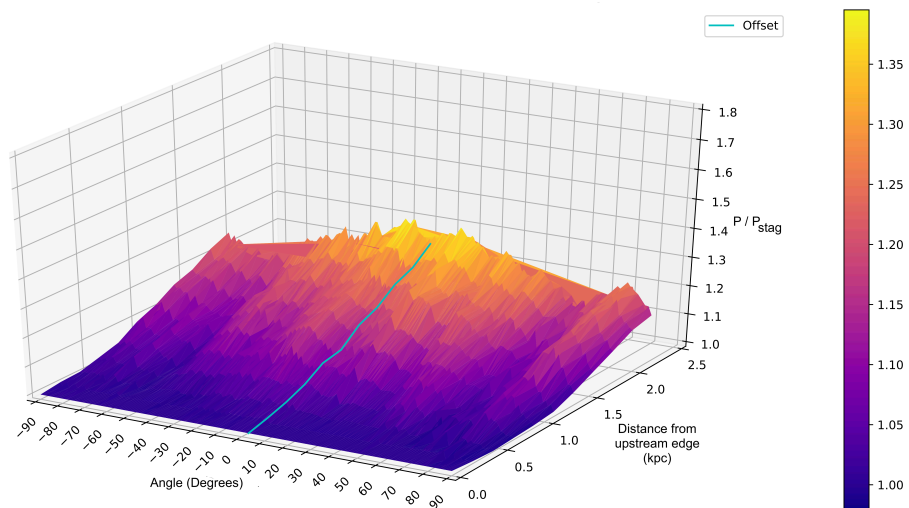
Figure 4.4: This figure shows how well the 3D model from [Su et al. \(2017b\)](#) fits the pressure profile along the upstream edge. This data is from 980Myr, during the first infall of [Sheardown et al. \(2018\)](#)'s V2 simulation. Pressure ratio (P/P_{free}) is plotted against angle θ along the upstream galactic edge of NGC 1404. The location of the stagnation point is shown by the grey vertical line. This figure also shows the polyfit that was applied to the data to define the location of the stagnation point, and the 3D method both with and without gravity. The 3D models were only fitted to the central ± 60 degrees from the stagnation point to avoid fitting issues from the tail/wake. Within approximately ± 45 degrees of the stagnation point, the 3D models give us a good fit to the data, with the stolen atmosphere model accounting slightly better for instabilities. The estimated velocity values from the two fitted models shown closely match their 2D equivalents.

weak to observe small features like the stagnation point. To combat this, observers assume hydrostatic equilibrium across the upstream edge, as the shape of galactic upstream edges is near-static during a stable infall, stating that $0 \approx 0'$ (Vikhlinin et al., 2001; Su et al., 2017b).

Figure 4.5 shows the pressure, as a ratio of the measured P_{stag} , inside the upstream edge of the galaxy at the current time for the V0 and V2 simulations. The thin blue line shows the offset, which is the line between the centroid and the defined stagnation point. These plots show that there is indeed a reasonable level of hydrostatic equilibrium across the upstream edge of the galaxy. However, the pressure quickly increases a small distance inside the boundary (about 0.5kpc in these cases), as we would expect from Figure 3.3. It forms a rough peak in the middle, closest to the gravitational potential centre of the galaxy. In a perfect theoretical universe, it would be possible to either probe the pressure for physically small space just inside or just outside the galactic boundary, but this is not possible in reality due to projection and telescope limitations. In the case of Su et al. (2017b), the bins used around the upstream edge of NGC 1404 have a radial height of 1.5kpc to 2.0kpc, and are significantly wide. Since the number of the photons is averaged across each bin, a rough estimation can be done to see what the effect of the bin size and location would be on these simulations. Assuming approximate linearity over the relatively small bin, any systematic overestimation would probably be equivalent to taking a point at $\sim 0.75\text{kpc}$ inside the boundary. This equates to between a $\sim 7\%$ to 15% increase in measured stagnation point pressure, depending on the width of the bins and which simulation NGC 1404 is most similar to in terms of interior structure. While this result is only a rough estimate, it is based on the best match of two tailored simulations and it illustrates the significant impact that the internal structure of a galaxy can have on the stagnation point method. It is especially important to consider this when applying the stagnation point method to galaxies that have a smaller angular size than NGC 1404, as the physical bin size will have an even larger effect.



Simulation V0



Simulation V2

Figure 4.5: Figure showing how the pressure varies inside the galactic boundary at the current time for the V0 and V2 simulations. These display the ratio of P/P_{strip} (where P_{strip} is the pressure at the upstream edge, along which the stagnation point sits) to show the effect that observing the stagnation point inside the upstream edge has on the values measured. The thin blue line shows the offset, which is the stagnation point according to the polyfit. The angle has been defined from the centroid in each case.

4.2 ICM Flow

4.2.1 Stable Flow

In order to classify the different periods of flow throughout the simulation, an ideal case must first be established. The linear-flow ram pressure stripping scenario outlined and analysed in [Roediger et al. \(2015a\)](#) is an excellent representation of the ideal flow scenario, in accordance with the assumptions made for the stagnation point method (i.e. consistent ICM variables and flow velocity). [Roediger et al. \(2015a\)](#) show a simulated galaxy in a consistent flow, repeated over a range of parameter changes that demonstrate the kinds of stable flow characteristics that can be used to help identify and understand stable flow in real scenarios. The most notable sign is that a galaxy in stable flow has the typical, linear head-tail morphology, with no significant asymmetry in the tail or upstream edge: there should be a smooth upstream edge and a near-tail at the opposite side to the sharpest upstream density discontinuity. Stable flow will have a smooth distribution of mass (both gas and DM) within the galaxy itself too, as significant sloshing in and around the cold core of a galaxy indicates current or recent flow instability. Additionally, the movement of the gravitational potential relative to the overall galaxy will affect the ICM, and therefore flow, around the galaxy.

Based on this understanding of stable flow, it can be stated that galaxies near the apocentre or pericentre of their orbits must have unstable flow. While it is difficult to accurately define where apocentre and pericentre are in observational data, due to the difficulty of determining the previous orbit of a galaxy that appears stationary in human time-scales, this is a general rule that may be useful to consider, as there are significant changes in both direction of travel and distribution of mass during these periods. Unfortunately, there is only a relatively short period of stable infall between apocentre and the second pericentre passage in the V0 and V2 simulations used here, making it difficult to analyse the second/third infalls with much confidence.

4.2.2 Classifying Periods of Flow

Each of the simulations can be split into periods of different flow characteristics:

1. The beginning of the simulations is dominated by initial conditions, so the flow must be allowed to settle before it can be considered steady. During this phase the stolen atmosphere is also being established. This can be seen in Figures 4.2 and 4.3, where $P_{\text{stag}} = P_{\text{free}}$ initially but from $\sim 500\text{Myr}$ onwards the simulated P_{stag} matches the estimated P_{stag} .
2. We deem the flow settled $\gtrsim 800\text{Myr}$ for V0, and slightly earlier for V1 and V2, based on visual assessment of density slices and confirmed by viewing the flow relative to NGC 1404's centre. After this comes a period of stable flow in which the ICM is largely undisturbed, allowing easy definition of free stream variables. In this period, there is strong agreement between the full stagnation point method (with compressibility and gravity) and the velocity taken from the simulation, which lasts nearly until pericentre passage. During this period, before pericentre passage of the the first infall there is disagreement of $\sim 400 \pm 50\text{km/s}$ between the simulation velocity and the method with compressibility, no gravity for all simulations.
3. Shortly after pericentre passage there is a period of unstable flow during which the centroid could not be consistently fitted to the now lumpy upstream edge, which also makes the stagnation point difficult to define, or, more precisely, the stagnation point itself is not well defined in this situation. It is important to acknowledge the luxury in terms of data quality, resolution, and the ability to take data directly from the plane of the merger that using simulations allows us. This means that applying the stagnation point method is significantly easier with simulation data than with observational data, but it still fails in this unstable flow phase. During this period, flow patterns are irregular around the galaxy, and this lasts until after apocentre when the next infall starts. Additionally, during this period of instability, background variables could not be found using the galactic edge to define a_{Az} (see Figure 3.4) - hence the discontinuities that occur between stable and unstable periods in Figures 4.2 and 4.3. While the change in background variable definition skews the results, it is clear that the systematic increase in the velocity estimated is a fairly minor factor in the significant velocity overestimation during this period, during which the velocity is sometimes estimated at

$> 3\times$ the actual value by methods that neglect P_{grav} . We found that the problems fitting a centroid reliably occurred at times of unstable flow, so we suggest that the smoothness of the upstream edge can be a useful metric when considering whether the stagnation point method should be applied. Further analysis of this period and its flow can be found in [Sheardown et al. \(2019\)](#).

4. After the period of instability around apocentre, the next infall starts, settling back to a stable flow. It is not trivial to define exactly the change between stable and unstable flow but we believe this can best be judged by the smoothness of the upstream edge, and the symmetry across a line drawn between sharpest density discontinuity along this upstream edge to middle of the near-tail. If it is possible to view a significant amount of the galaxy's tail, it may be possible to identify the change from slingshot tail to ram pressure tail that signifies the beginning of a new infall, as shown in Section [5.2](#)

The best match to current observations is marked on each of Figures [4.2](#) and [4.3](#). The 'current time' for simulation V0 is at 2790Myrs, and for simulation V2 it is at 3590Myrs.

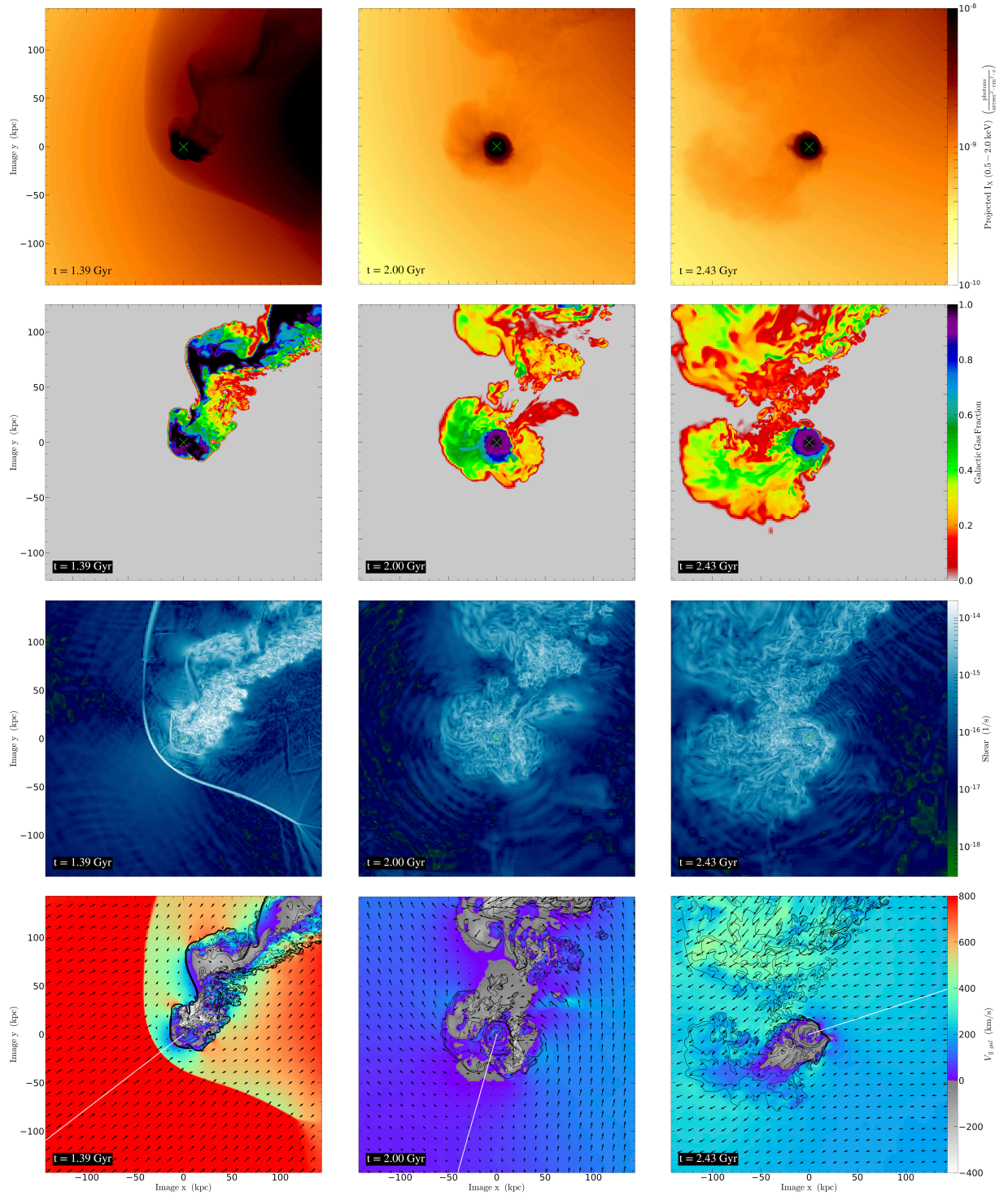
In all simulations the analysis was run only for the first two infalls because the free stream variables become too difficult to consistently define beyond this point, due to global motion in the ICM triggered by the earlier infalls of this one galaxy.

4.2.3 Slingshot Tails

These figures show the early, mid, and late stages of slingshot tail development for the two modes of slingshot tail: overrun and arc-shaped. At each stage, a projected X-ray intensity map is shown, along with the galactic gas fraction slices to show mixing, plus shear and velocity maps to show how the flow is evolving. The shear shows where significant velocity changes occur, which helps highlight instabilities and mixing, and the velocity map shows the velocity parallel to the white line that traces the direction of velocity from the galaxy centre. The velocity map also has arrows to show the overall flow relative to the galactic centre.

In Figure [4.6](#), the galaxy is first shown shortly after pericentre passage, and the next two columns show Phase 1 and Phase 2 of the overrun slingshot tail respectively. The galactic

Overrun slingshot tail



(a)

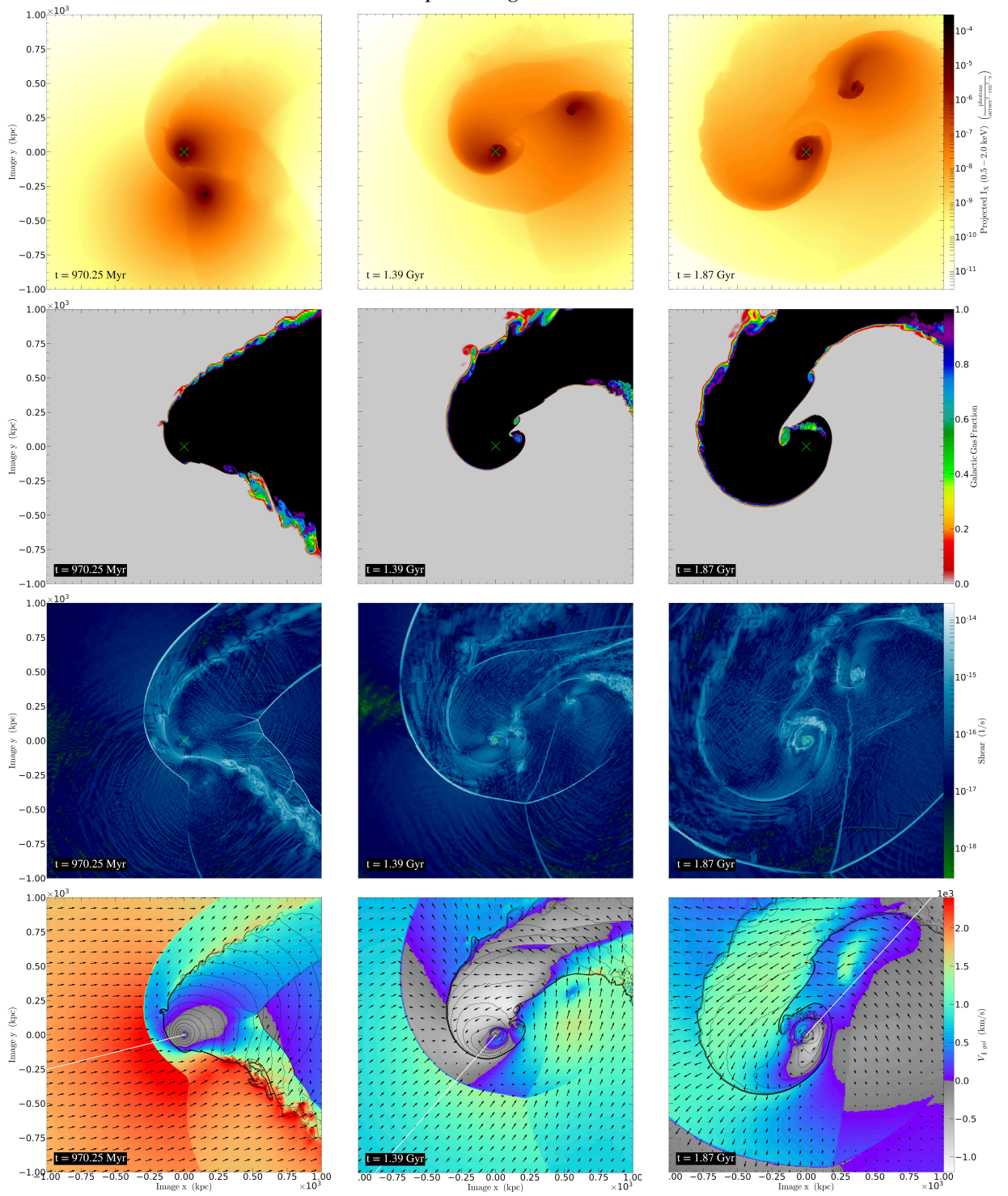
(b) Phase 1

(c) Phase 2

Figure 4.6: The aim of this figure is to show the flow patterns in and around clusters with *overrun slingshot tails*. The images are made from the V1 simulation in Sheardown et al. (2018), the same simulation as the two left-hand columns of Figure 2 of Sheardown et al. (2019). Each column shows an X-ray photon intensity projection in the orbital plane; a gas fraction slice of the galaxy, showing the extent to which the tail has been stripped and mixed with the ICM; a slice of the shear rate, showing the locations of strong shear flows; and finally a colormap of the flow field, overlaid with velocity vectors. For the latter, the colormap codes the velocity component $V_{\parallel gal}$ parallel to the galaxy's direction of motion, in the rest frame of the galaxy. The white line from the galaxy centre shows the direction of motion of the galaxy with respect to the grid and the contours show the gas density of the galaxy's atmosphere as it is stripped. The rainbow part of the colormap shows gas flow toward the galaxy's downstream direction, while the grayscale part shows the flow toward the upstream direction.

The images in Column (a) show the unstable flow beginning to develop. (b) shows the galaxy near apocentre as the *overrun slingshot tail* is in the first phase with an irregular shaped atmosphere. (c) shows the flow shortly before it becomes classed by this paper as a stable infall again, where now we have phase two of the *overrun slingshot tail* as a conical tail develops behind the galaxy. Both (a) and (c) can both be considered fringe cases in terms of the flow stability. This figure demonstrates that during the creation of a slingshot tail, the galaxy undergoes a significant asymmetrical flow relative to its direction of motion - even in the case of (c), which may be considered steady based on X-ray observations.

Arc-shaped slingshot tail



(a)

(b)

(c)

Figure 4.7: This figure shows similar images to Figure 4.6, but for an *arc-shaped slingshot tail*. These images are taken from the 3:1 merger simulation shown in the two right-hand columns of Figure 2 of [Sheardown et al. \(2019\)](#).

The images in Column (a) show the unstable flow beginning to develop, with a particularly asymmetric flow beyond the shock front due to the location of the cluster's BCG. (b) shows the galaxy near apocentre, midway through the development of the slingshot tail; the galaxy's tail starts to create an arc, as the outer edge of the tail is pushed out beyond the galaxy. (c) shows the flow shortly before it becomes classed by this paper as a stable infall again.

gas fraction in particular shows how the remnant tail engulfs the galaxy, before being left behind in the cone-like tail. It also makes it clear that an upstream edge and stagnation point do not actually exist in that phase. As explained in [Sheardown et al. \(2019\)](#), the overrun slingshot tail can be split into two main phases. In Phase 1, the galaxy slows as it turns, and is overrun by the remnant tail of unmixed galactic gas that is downstream of it. In Phase 2, the galaxy speeds up towards the cluster centre, leaving behind a cone-shaped tail made up of this overrun remnant tail. These phases will be discussed further in §5.2.1.

5. Discussion

“Hello, IT. Have you tried turning it off and on again?”

– Chris O’Dowd as Roy Trenneman, *IT Crowd* (2006)

5.1 Stagnation Point Methods

In this thesis, we analysed an idealised N-body + hydrodynamic simulation of a minor cluster merger between a host cluster and a massive elliptical galaxy. The aim of our analysis was to determine whether the stagnation point method is a valid method for estimating the velocity of the galaxy within the cluster throughout the merger. Our analysis of the validity of the stagnation point method revealed two key points:

- There are phases of a minor merger where *no* version of the stagnation point method can be applied to estimate the galaxy’s infall velocity. These are phases at and after pericentre until after apocentre passage. During these periods, the ICM flow around the galaxy is rapidly changing or highly unstable.
- During infall phases, the stagnation point method can estimate the galaxy’s velocity much more accurately if the effect of the galaxy’s gravitational potential, i.e. the stolen atmosphere effect, is taken into account.

These two points will be discussed in more detail below, along with other aspects.

5.1.1 When the Stagnation Point Method Cannot Be Used

We find that there are three significant factors that cause the stagnation point methods to break down at pericentre:

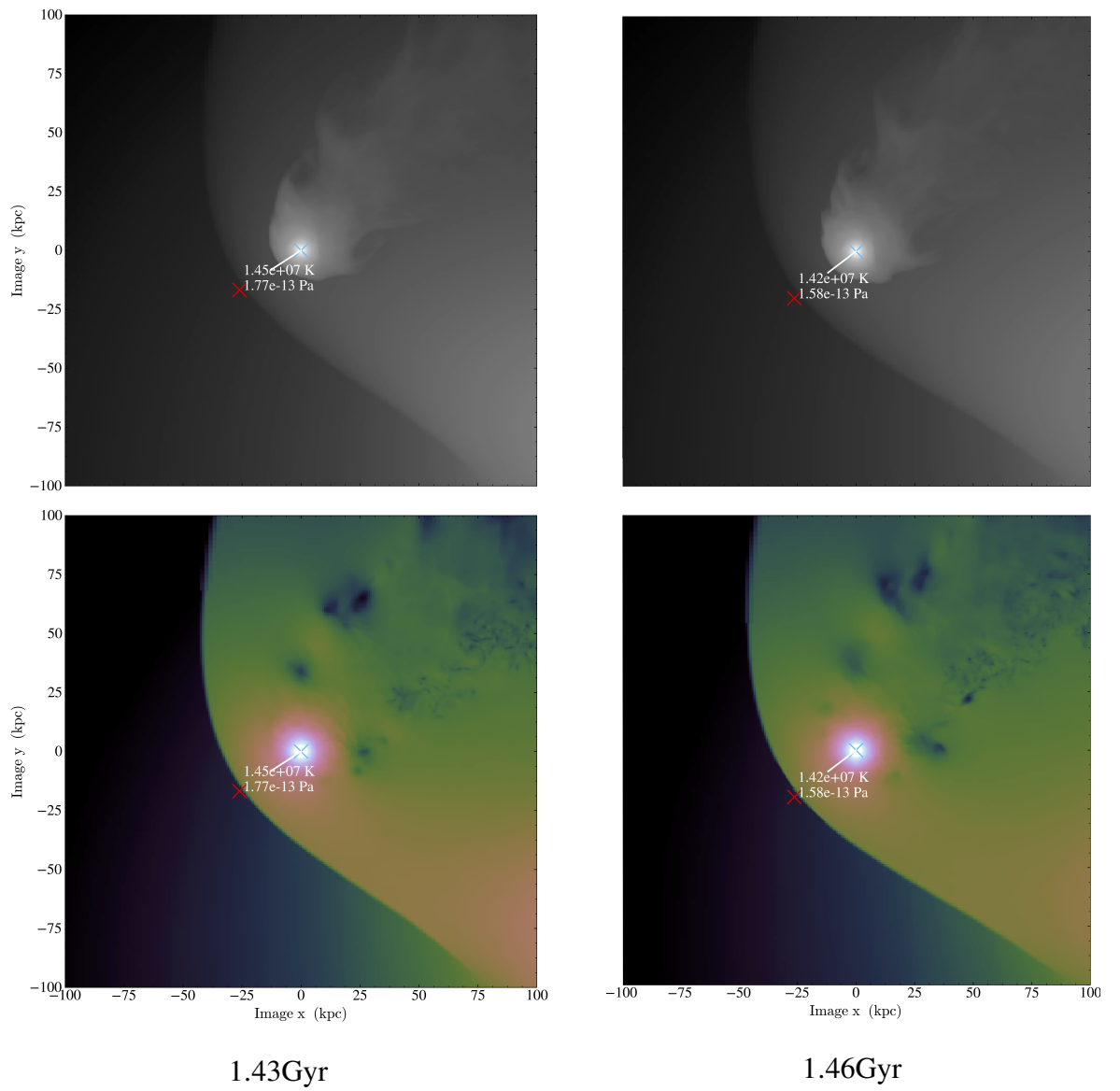
- There are significant ICM (P , T and ρ) gradients near the galaxy when it is close to the cluster centre. Therefore, the flow changes too quickly to be approximated as steady

and the free stream variables become more difficult to define. We note that in the stolen atmosphere model, P_{grav} relies particularly heavily on the accurate definition of T_{free} , so any T_{free} uncertainty has an additional impact.

- There is more significant sloshing in the ICM near to the cluster centre, as well as potential shock fronts from the cluster centre, further disrupting steady flow.
- Significant changes in both the speed and direction of the galaxy occur as the galaxy passes close to the centre of the cluster potential. This causes a disruption in flow (asymmetry) and the internal structure, both of which reduce the suitability of the stagnation point method.

Shortly after pericentre passage, the velocity from the stagnation point method with compressibility and gravity no longer has a good agreement with the simulation value. Figures 4.2 and 4.3 both show a good agreement between the simulation and the estimate of P_{stag} from our new model after the respective first pericentre passages of V0 and V2, but the ratio $P_{\text{stag}}/P_{\text{free}}$ drops significantly due to overestimation of the free stream variables. Unfortunately this makes sense with the definition of the free stream variables used, as the azimuthal average around the cluster core is now being taken at the downstream edge¹, which is currently the closest galactic edge to the cluster centre. It would be useful to adapt the definition of the free stream variables but due to time limitations, and for the purposes of keeping the definition simple, this has not been done. Instead, some manually chosen free stream locations were chosen after the first pericentre passage of V2. V2 was chosen due to the supersonic motion after pericentre passage constraining much of the compression past the bow shock, allowing a free stream location to be picked just upstream (within $\sim 2\text{kpc}$) of the shock (see Figure 5.1). Unfortunately, it was not possible to pick free stream locations this way for V0 as it lacked the shock post-pericentre passage that separates the region of compression from the uncompressed ICM.

¹This is due to the method of defining free stream variables using a value based on data points around a circle around the cluster centre defined by the distance between the cluster centre and the closest edge of NGC 1404 (see Fig. 3.4d).



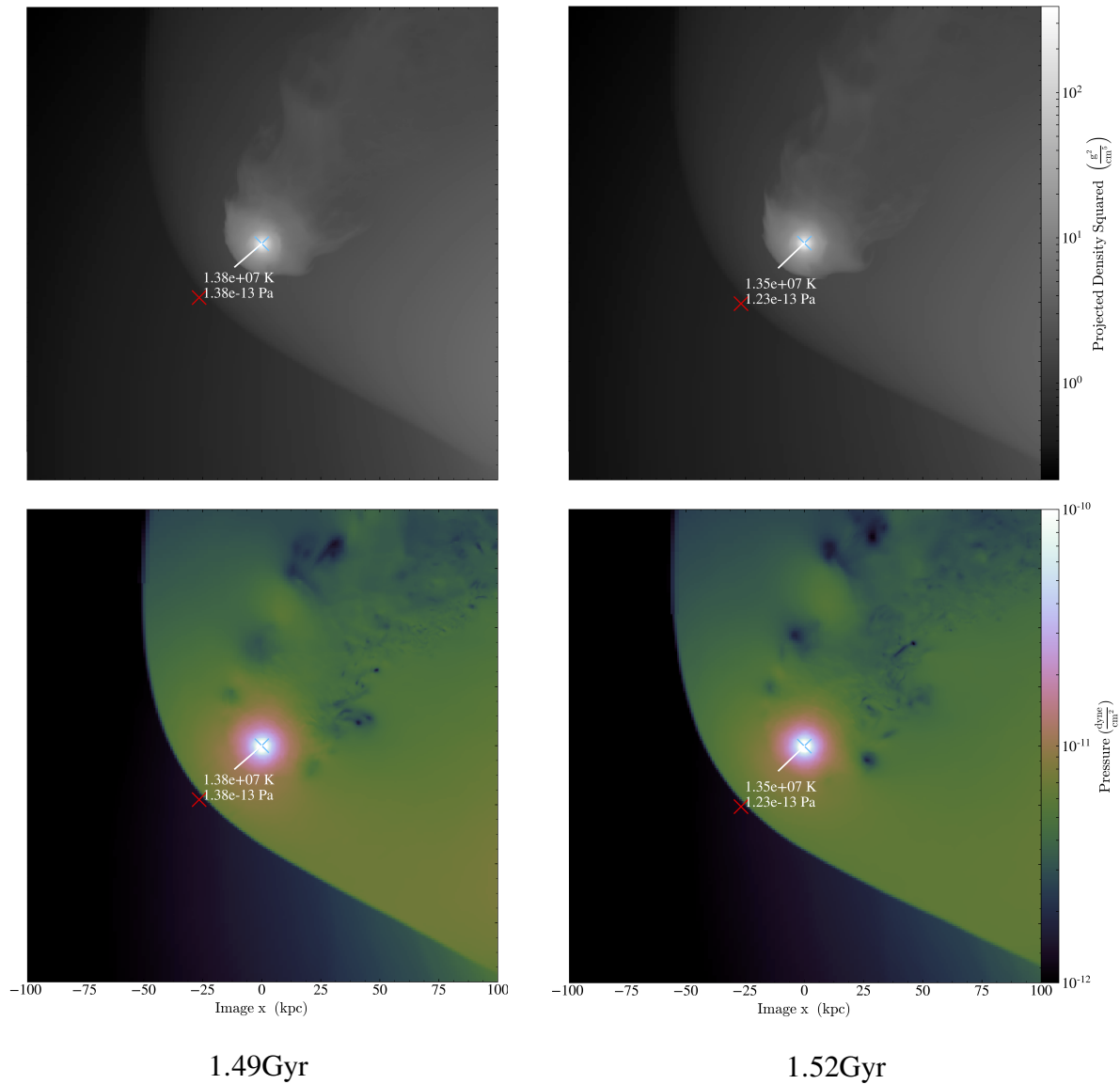


Figure 5.1: Slices of pressure and approximate emission showing the manually defined free stream locations after pericentre passage of the V2 simulation. The projected density squared gives a view of what the situation would look like to X-ray telescopes. The pressure data shows how strongly the compression drops off beyond the bow shock, and how the ambient ICM pressure gradient fades at the bottom right as the galaxy passes the cluster centre. In particular, the combination of these two pressure gradients, with the galactic velocity not being aligned with the gradient, illustrates the difficulty in defining the free stream variables in such situations.

The locations chosen in Figure 5.1 are certainly not perfect as they are significantly further from the cluster centre than the galaxy is, introducing a systematic underestimation of the free stream variables (leading to an overestimation of velocity). The locations used also ignore the relatively small amount of compression that occurs upstream of the bow shock, which may counter the free stream underestimation to a small extent. However, the closer to the galaxy that the data points are placed, while still being beyond the bow shock, the better the velocity estimation, implying that the ICM gradient is more significant than the compression beyond the shock. While these few plotted points are not statistically significant and are reliant on human judgement rather than an algorithmic approach, they do show the sensitivity of these models to uncertainty in the free stream variables and highlight the statistical issues with the main method for free stream definition used.

The disturbance to steady flow that occurs at pericentre passage can be linked — through the asymmetries that develop — to the long period of considerable fluctuation in velocity estimation, and therefore the stagnation point method’s inaccuracy around apocentre. These asymmetries can develop into a slingshot tail (Sheardown et al., 2019). The highly irregular flow patterns around apocentre make the application of the stagnation point method unsuitable, as they rely on the solid body in a free-stream analogue. This chaotic flow also makes it difficult to reliably define anything resembling a stagnation point or centroid, even in the plane of the merger with all the data availability of a simulation.

5.1.2 Including Gravity

Our results show that current stagnation point methods, which neglect the contribution of P_{grav} , systematically overestimate the infall velocity. As expected, the effect is less significant for higher velocities, but even at the highest velocities in the simulations tested, an error of $\sim 400\text{km/s}$ remains. This thesis uses the stolen atmosphere effect from Roediger et al. (in prep.) to describe the gravitational enhancement of the ICM pressure near the galaxy. It is important to remember that, whereas the ICM requires time to react to the galactic potential, the stolen atmosphere model assumes the enhancement is instantaneous, unless further complexity is added. As a result, Eq. 2.7 will overcorrect for P_{grav} when the stagnation point method with compressibility and gravity is applied to extreme infall velocities ($\mathcal{M} \gg 1$).

However, with most infall velocities, including those of NGC 1404 during the simulations, this will not be an issue.

Having a good understanding of the gravitational potential of the galaxy/subcluster being observed is crucial for the application of the new stagnation point method with compressibility and gravity. This is made clear in the second infall of Figure 4.3, where there is a significant difference between the estimated velocities depending on whether the initial gravitational profile is assumed to be consistent throughout the simulation or the gravitational potential values are dynamically extracted from the simulation. As not much mass was lost between the first and second infalls, this difference between methods can largely be attributed to a change in mass distribution. As a disturbed gravitational field will affect the internal structure and flow around the galaxy, which will in turn affect gas stripping, the application of the stagnation point method may not be appropriate even long after pericentre or apocentre passage (or at least should only be considered with some caveats). The application of the method with gravity has to be based on certain assumptions (e.g. the observational estimation of gravitational potential requires assumptions about the mass distribution), and as the gravitational potential can have significant perturbations long after the flow would otherwise be considered stable, it is very difficult to confidently analyse the velocity of a galaxy using the stagnation point method. Because most galaxies will have undergone some significant interactions with other bodies before their current merger, it could be worth calculating the gravitational relaxation time of the galaxy in question in relation to nearby bodies, to help quantify uncertainties around this method.

5.1.3 Additional Sources of Uncertainty

While we have tailored our analysis to observational methods where appropriate, and have already considered several factors that contribute to systematic errors, we have avoided focusing on specifics relating to the observation process. There are four main potential sources of uncertainty that should be considered and studied further for the application of the models discussed in this thesis:

- The stagnation point is observationally defined by the sharpest visible edge (Vikhlinin et al., 2001; Su et al., 2017b), which should align with the point of highest pressure along the upstream edge that we used. This assumes the merger is occurring in the plane of the sky with minimal projection effects. The 3D model used here allows us to model the actual stagnation point pressure of mergers that occur out of the plane of the sky, though great care must be taken in its application as relatively small instabilities can cause significant systematic errors.
- The stagnation point pressure is generally observationally determined inside the galactic boundary as this region is brighter and it is generally assumed that $P_{\text{stag}'} \approx P_{\text{stag}}$ based on pressure equilibrium arguments (Vikhlinin et al., 2001; Su et al., 2017b). However, it is likely that this will cause a slight velocity overestimation as the gravitational pull causes a pressure gradient towards galactic centre (from Figure 4.5, we estimate that the stagnation point pressure would be overestimated by $\sim 10\%$ to 15% at the current time from simulations V0 and V2) — though this will be dependent on the dimensions of the bin(s) used, projection, angle of infall, etc. Overall, this is likely to be a minor influence in comparison to the other systematic factors.
- The stolen atmosphere model is particularly sensitive to the gravitational potential of the galaxy (power of 2.5 in Eq. 2.7). Given this and the uncertainty in observational mass measurement (Takizawa et al., 2010; Vikhlinin et al., 2006; Shi et al., 2016), the gravitational potential will be a significant, if not dominant, source of uncertainty in velocity estimation of a galaxy when including gravitational pressure through the stolen atmosphere effect.
- The way that the free stream variables are defined:
 - If defined close to the infalling galaxy, free stream values can be ‘contaminated’ by the stolen atmosphere.
 - If the the azimuthal averaging radius a_{Az} around the cluster centre is reduced, the velocity that the models predict is significantly reduced (see the discontinuities between stable and unstable regions in Figures 4.2 and 4.3). The significant

effect of a poor free stream definition can be seen in Figure 4.3 by comparing the velocity estimated using manual free stream definition (as shown in Figure 5.1) to the velocity estimated using the regular free stream definition used in this thesis.

- Sloshing can cause further disagreement between the background values measured and those being ‘experienced’ by the galaxy. The issues fitting the stagnation point methods around the second infall can be attributed to this, as some significant asymmetries in the ICM that affect the free stream variables can be seen at this time.

5.1.4 Velocity of NGC 1404 Through Fornax

Current velocity estimates for NGC 1404 do not account for the stolen atmosphere effect, so will be overestimates if all other aspects of the analysis are correct. Using the potential model from Sheardown et al. (2018) in the simulations, most of the time $P_{\text{grav}} > P_{\text{ram}}$. Closer to pericentre, the ram pressure increased until $P_{\text{grav}} \approx P_{\text{ram}}$. The potential model from Sheardown et al. (2018) does a reasonable job of describing the NGC 1404 potential, since it has separate DM and stellar components, so it can be used for some simple estimates. While in previous analyses (e.g. Su et al., 2017b; Machacek et al., 2005a) the enhancement of the stagnation pressure over the free stream pressure was solely attributed to P_{ram} , our results imply that only half of this enhancement should have been attributed as such since NGC 1404 is currently approaching pericentre passage. Using this ratio with the simple stagnation point method without compressibility (Equation 2.4), where:

$$P_{\text{ram}} = \frac{1}{2} \rho_{\text{free}} v_{\text{free}}^2$$

we can say that if P_{ram} was overestimated by a factor of 2, the velocity was overestimated by a factor of $\sqrt{2}$. Thus the velocity estimate should be reduced by a factor of $1/\sqrt{2} \approx 0.7$. As the estimated velocity of NGC 1404 is near Mach 1, using the compressible version of P_{ram} should result in a similar correction (see Figure 2.3).

We note that for a better estimate of infall velocity, the potential of NGC 1404 needs to be modelled very carefully as P_{grav} is very sensitive to the potential (see Equation 2.7). Due to

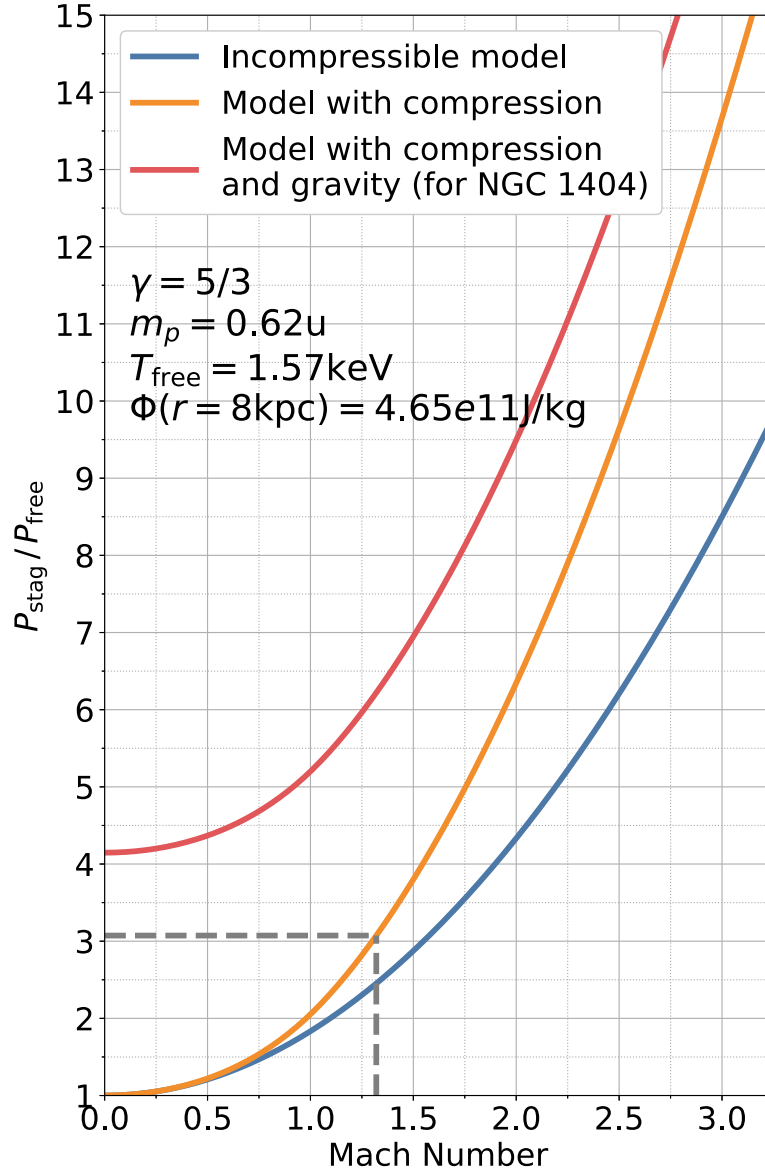


Figure 5.2: Plot comparing the relation between the $P_{\text{stag}}/P_{\text{free}}$ pressure ratio and the predicted Mach number for different stagnation point methods. This plot is the same as Figure 2.3 with an additional line showing an estimated modification for gravity using the new stagnation point method (Equations 2.9 and 2.10). As the stolen atmosphere modification relies on the free stream temperature and gravitational potential at the stagnation point, the relation between pressure ratio and Mach number cannot be generalised for this method. Therefore, this result is specifically for NGC 1404, using a free stream temperature of 1.57keV from Su et al. (2017b) and gravitational potential energy from the simulation (Table 3.1) with a radial distance between galactic centre and stagnation point of 8kpc. We used an average ICM particle mass of 0.62 atomic mass units. The Mach value and corresponding pressure ratio from Su et al. (2017b) has been plotted for comparison.

P_{grav} relying on the free stream temperature and the gravitational potential at the stagnation point (or upstream edge if using the 3D variant), the new method cannot be compared to the other stagnation point methods as simply as in Figure 2.3. However, a simple case can be created using sensible values for NGC 1404. Using an average ICM particle mass of $0.62u$ free stream temperature of $T_{\text{free}} = 1.57\text{keV}$ (Su et al., 2017b) with a radial distance between NGC 1404's centre and the stagnation point of $r_{\text{strip}} \approx 8\text{kpc}$ and the gravitational potential in Table 3.1, it is possible to plot the relation between $P_{\text{stag}}/P_{\text{free}}$ and Mach number for the new model. This is shown in Figure 5.2, which is an equivalent of Figure 2.3 with an additional line for showing this model. This makes it very clear that something must be wrong with the values used as the Mach number found by Su et al. (2017b) (plotted in Figure 5.2) of $\mathcal{M} = 1.32$ corresponds to $P_{\text{stag}}/P_{\text{free}} = 3.07$ (using the 2D equivalent of the stagnation point method used in Su et al., 2017b), which less than if the only enhancement over P_{free} was due to gravity according to our calculations ($P_{\text{stag}}/P_{\text{free}} = 4.15$). This may be due to the gravitational potential value used. It is also possible that the free stream variables used were contaminated by the stolen atmosphere effect, although this is unlikely to account for the entire difference.

It is very likely that that NGC 1404 is not experiencing steady flow because of the ICM sloshing produced during its previous infall(s). While we do find that the model with compressibility, no gravity is in reasonable agreement with the velocity at the current time of the V0 simulation, we attribute this to ill-defined free flow variables, so we cannot recommend using this method near pericentre passage. One possibility is to properly account for these ICM gradients when modelling the compression region/shock front. This would reduce the physical distance over which the flow must be steady. Some work has been done by Zhang et al. (2019) using smoothed particle hydrodynamics simulations to assess the effect of such gradients, as well as acceleration, on the upstream shock fronts of galaxies. While their analysis was more focused on the standoff distance and on measuring the Mach number directly from the shock characteristics, it does suggest that more complex modelling of the upstream region may be possible. Also, it would be interesting to see whether these two approaches for estimating galactic speed could be combined to better constrain velocity.

5.2 Misleading Slingshot Tails

For simplicity, in the following section the smaller body in the minor merger is referred to as the galaxy, while the larger body is called the cluster. However, the analysis also applies to a subcluster merging with a cluster. The following section (§5.2.1) has been modified from the text that I contributed to [Sheardown et al. \(2019\)](#).

5.2.1 Flow Patterns

Ram pressure tails or slingshot tails have recently attracted interest as locations to study turbulence or its suppression in the ICM ([Roediger et al., 2015b](#); [De Grandi et al., 2016](#); [Eckert et al., 2017](#)). To do so, it is important to understand the principal flow conditions in and around such tails. Furthermore, regular flow patterns around the galaxy are a prerequisite to the meaningful application of the stagnation point method to determine the galaxy’s velocity ([Vikhlinin et al., 2001](#); [Su et al., 2017b](#)). In what follows, we show that this method is not applicable to clusters producing slingshot tails due to their complex flow patterns which differ from the pure ram pressure scenario.

The genesis of a slingshot tail can be split into two periods, which we show in Figures 4.6 and 4.7. In the first period, right after pericentre passage, the galaxy continues to drag a significant amount of its downstream atmosphere along as a remnant tail. As the galaxy slows and changes direction approaching apocentre, the remnant tail is carried by its momentum and its attraction to the galaxy’s gravitational potential as it falls back toward the remnant atmosphere of the galaxy. At this point, there is significant flow within the remnant tail tangential to the galaxy’s direction of motion, with similar flow patterns regardless of the form of slingshot tail.

The flow patterns in the second period are complex and potentially misleading. The galaxy either develops into an *arc-shaped slingshot tail*, (Figure 4.7b), or develops into an *overrun slingshot tail*, (Figure 4.6b), as the tail begins to fall back and wash over the galaxy. For the latter, the remnant tail washes over the galaxy causing a ‘false’ head-tail shape to form (i.e. a head-tail that does not represent the motion through the ICM); this is the process which generates the conical tail of the *overrun slingshot tail*. Additionally in this process,

the overrunning tail causes some stripping of the remnant atmosphere of the galaxy, adding to the ‘false’ head-tail shape. In this state, the appearance of the galaxy is misleading when determining the direction of motion and merger history. An example of this is shown in Figure 4.6b, where the sharpest edge in the X-ray plot may naively suggest a roughly north-easterly direction of motion, even though the galaxy is moving to the south. Additionally, this process disrupts the internal structure of the galaxy, as its atmosphere sloshes around its potential.

As mentioned, the beginning of the flow for both slingshot forms is similar, but there are some key differences. One such difference can be seen when comparing rows 2 and 3 in Figures 4.6 and 4.7. In the *arc-shaped* form, the galaxy’s tail holds significantly more of its own gas through pericentre passage, with an area of laminar flow following the galaxy within the tail. This laminar flow appears to translate to the smooth arc-shaped edge in Figure 4.7b,c. Conversely, the *overrun* form shows a much more turbulent/broken tail (see Figure 3.5, rows 1 and 2 for a wider view of the simulation), perhaps better described as a wake at later stages, as the galactic gas is now well mixed with ICM. This is made obvious when comparing the shear rate in both slingshot forms. For the *arc-shaped* form, we see that there is significantly less shear in comparison to the *overrun* form as the tail gas co-moves with the ICM and the turbulent regions of the tail at the outer edge are mostly shed as the galaxy reaches apocentre. We note that an *arc-shaped slingshot tail* can be more turbulent if the galaxy does not manage to retain such a large amount of its own atmosphere past its pericentre passage, for example Hydra A (De Grandi et al., 2016).

As the galaxy moves away from apocentre, starting its next infall into the cluster, the flow patterns return to the steady flow state of the ram pressure scenario (Figures 4.6c and 4.7c). Figure 4.6c shows the *overrun tail* during the second phase as the flow begins to return to the ram pressure scenario. The flow here is fairly stable, but retains some asymmetry from the internal disruption/sloshing of the galaxy and the bulk motions of the ICM; this image is chosen to illustrate the difficulty in judging whether the flow is steady.

It is worth noting that the stagnation point method (Markevitch et al., 2000; Vikhlinin et al., 2001; Su et al., 2017b) to determine a galaxy’s velocity from stagnation point pressure

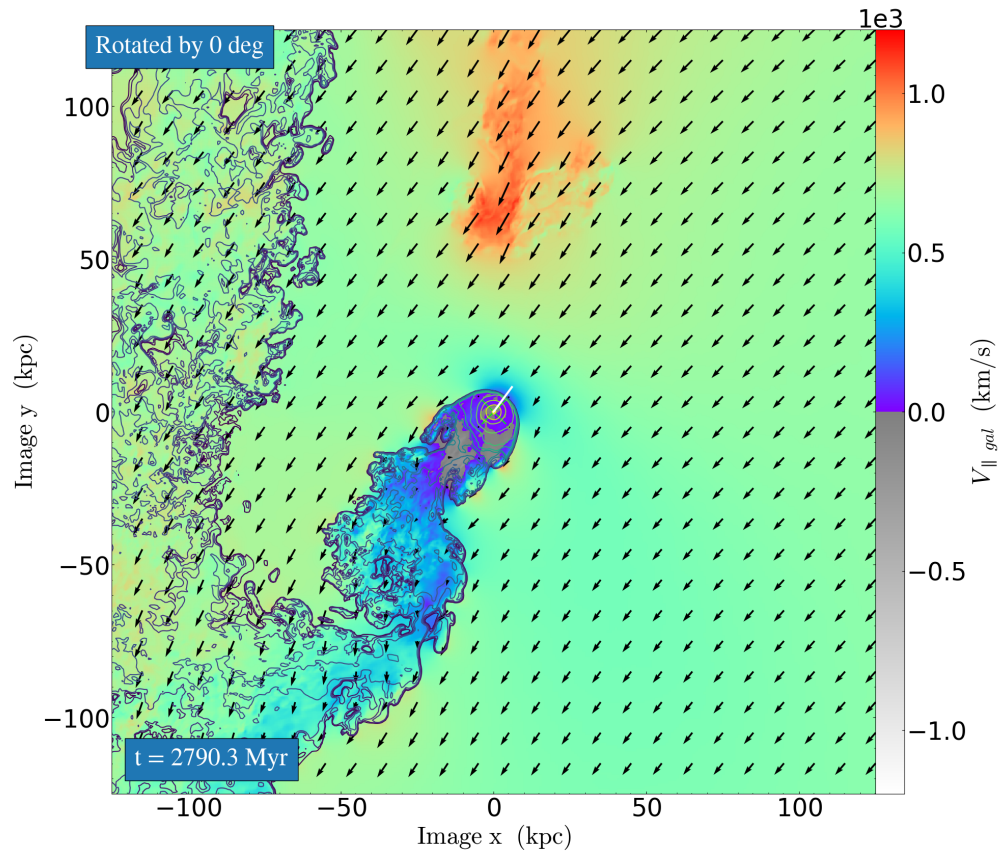


Figure 5.3: An example of the v_{\parallel} velocity field plot from the current time of the Sheardown et al. (2018) V0 simulation. This shows the mix of stable and more subtle unstable features that create difficulty when it comes to applying the stagnation point method.

relies on the analogy of a (quasi-)stable flow past a blunt body. The merger stage prior to and near pericentre passage would qualify for this, with columns (a) in Figures 4.6 and 4.7 showing borderline cases. However, around apocentre the flow patterns in the ICM around the galaxy are quite different and the stagnation point method is not applicable. Only when the regular flow patterns have been re-established during the next infall can the stagnation point method be applied again.

5.3 Flow Relative to a Galaxy

For the purposes of analysing the flow when it is steady or unsteady, it was important to be able to simultaneously see the magnitude of the velocity relative to the direction of motion and the directions of the flow in the ICM. Figure 5.3 shows an example of this at the current time of the V0 simulation, where the white line from the galactic centre shows the direction

of motion relative to the simulation grid and the colourmap shows the magnitude of the flow opposing this direction, relative to the galaxy. The quiver arrows show the direction and magnitude of the flow relative to the galactic centre, and contours have been plotted to show the density of the galactic gas. This method of visualising the flow relative to the infalling galaxy and stripping of the galactic gas has been used to confirm the flow's stability and analyse the mechanics of slingshot tails in §4.2.3. This view of the flow shows a largely stable upstream with a slight asymmetry relative to the direction of velocity, as in [Roediger & Brügger \(2006\)](#). Additionally, there is a significant amount of variation within the galactic atmosphere indicative of a sloshing core and unstable gravitational potential. While the immediate tail does not indicate any issues, the longer tail/wake shows significantly turbulent flow in its recent past, leaving behind a slingshot-like tail. Minor issues like these are likely not easy to observe, so may be overlooked, yet they have a potentially significant impact on the velocity estimated and our understanding of the bigger picture. However, it may be possible to account for them by carefully analysing a single point in time, rather than using the algorithmic method applied here — although this can introduce additional biases, so it must be done with caution.

5.3.1 Direct Line-of-Sight Velocity Observations

With future missions such as Athena, it will be possible to achieve an increased spectral resolution and therefore to map relatively small line-of-sight velocity features, i.e. the velocity perpendicular to the plane of the sky, as laid out in the NASA white paper [Su et al. \(2019\)](#). This should show any internal galactic sloshing as well as providing a new method to constrain infall angle relative to the plane of the sky. To visualise this, a projection map of z-velocity, or receding velocity, was made of V2 at the current time, Figure 5.4, to show the kind of detail this can hopefully reveal. This shows a significant bias between the left and right velocities, apparently rotating through the z-axis, suggesting that the mass distribution is unstable, which would fit with the results in Figure 4.3. There is also potential to see smaller features within the ICM, according to [Su et al. \(2019\)](#), allowing for a better understanding of ICM stability and improved free stream definition, though even the perfect view provided by the simulation did not make it easy to pick a good location.

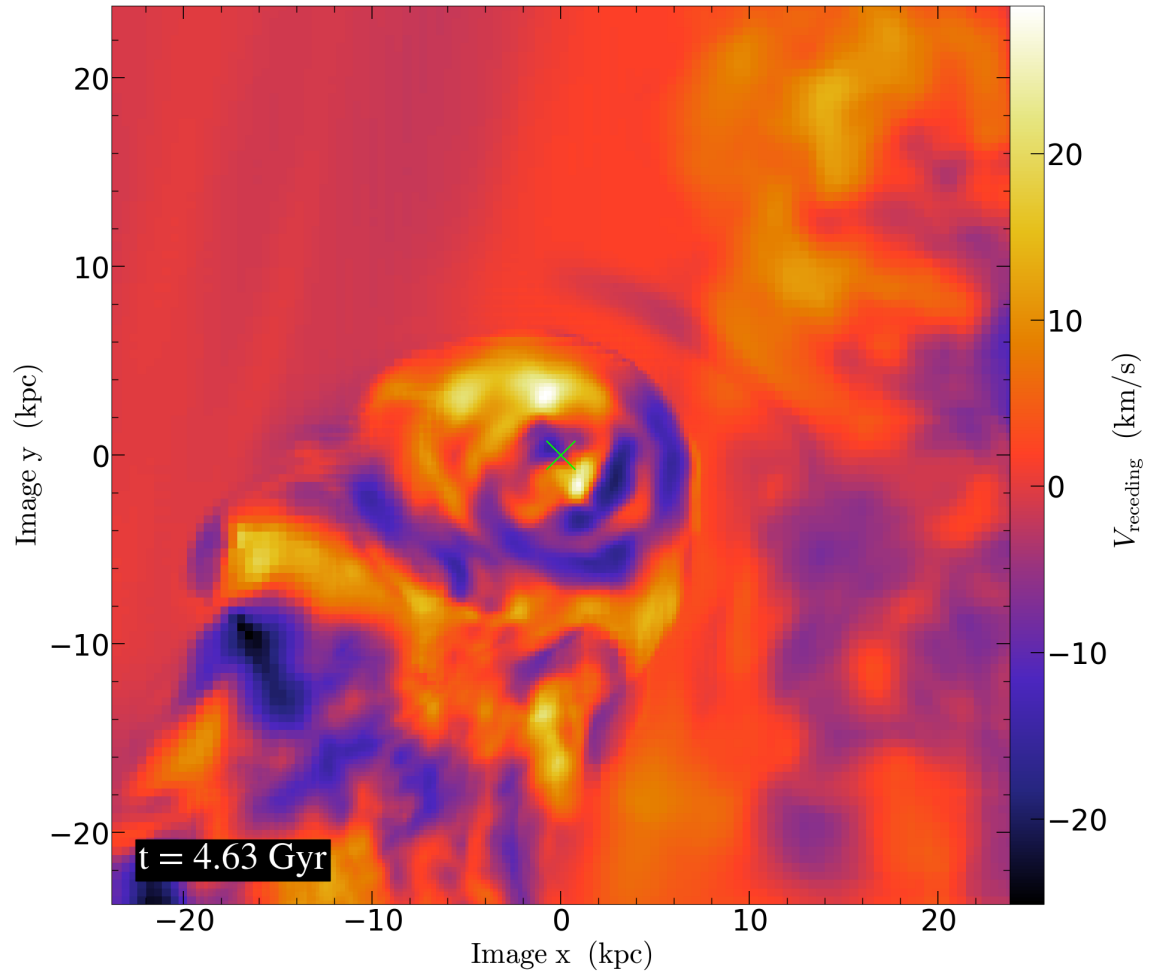


Figure 5.4: A map of line-of-sight velocity, i.e. velocity along the z-axis, weighted by X-ray intensity. This shows the V2 simulation at the current time, with a green cross to mark the galactic centre.

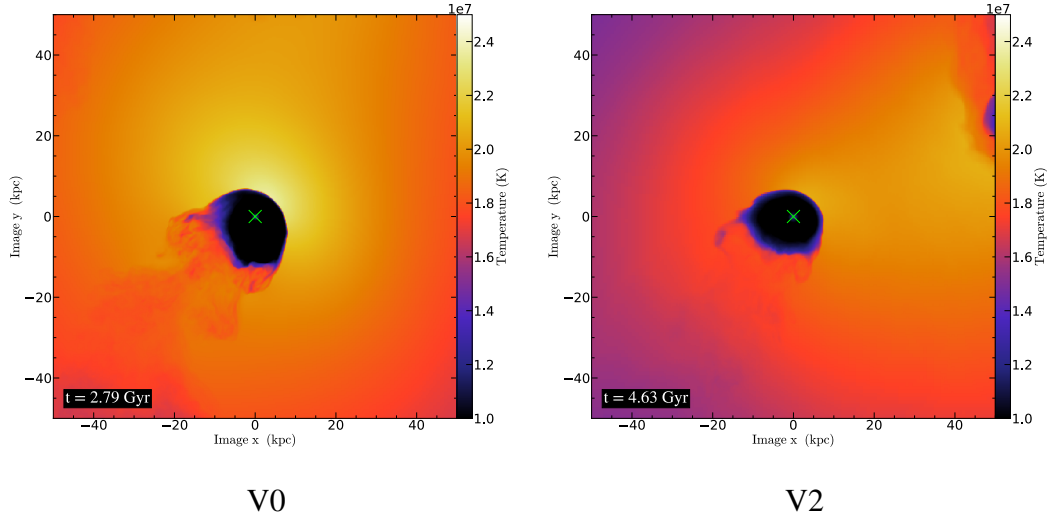


Figure 5.5: Temperature projection plots weighted to show observation-like values, applied to the V0 and V2 simulations at their respective current times. They each have a green cross to mark the galactic centre and are at the same scale, in order to make it a fair comparison.

5.4 Observing the Stolen Atmosphere

While it will be difficult to see the compression due to the stolen atmosphere effect in current observations, especially given projection effects, it may be possible to observe the halo of gravitationally heated gas that can be seen in Figure 3.3c. Although this halo could not be found with current NGC 1404 data, it may be possible to observe it in the future with improved instrumentation and techniques, if it is not hidden by projection effects. In order to test the viability of this, a temperature projection image was created using weighting from the following equation from [Rasia et al. \(2005\)](#).

$$T_{\text{sl}} \equiv \frac{\int \rho^2 T^a / T^{1/2} dV}{\int \rho^2 T^a / T^{3/2} dV} \quad (5.1)$$

where $a = 0.75$

In Figure 5.5, the V0 simulation image shows a clear temperature enhancement that peaks at the upstream edge, as predicted by the stagnation point equations, but also extends around the sides and to the downstream edges of the galaxy. Such a clear enhancement would be an ideal form of evidence to support the extent of the gravitational pressure enhancement that we predict. However, this figure shows the galaxy in a fairly relaxed ICM after only one

infall; it may not be realistic to find such a clear enhancement in a more complex system. In contrast, the V2 simulation image is much harder to parse, with a significant enhancement in temperature coming from the movement of the cluster centre and a ‘bubble’ of temperature-enhanced ICM appearing to surround the left half of the galaxy, possibly due to the stolen atmosphere effect. We also note that the stolen atmosphere heating occurs in the location where a bow shock would be expected in the case of supersonic motion. As a result, both phenomena may appear similar except for the sharp jump in pressure across the shock edge itself, if the instrument can capture this discontinuity.

6. Summary & Future Work

"I am 100% certain that I am 0% sure of what I'm going to do."

– Rob Lowe as Chris Traeger *Parks and Recreation* (2013)

6.1 Stagnation Point Methods

We find that the stagnation point method is not valid for certain epochs of a minor merger. From shortly before pericentre passage until after apocentre passage, the flow was too disrupted to be classed as stable in the case of our Fornax simulations. However, the periods of stable infall through settled ICM did give good results with our new stagnation point method. We find that the current models for applying the stagnation point method lead to a significant systematic error stemming from the assumption that the gravitational potential of the infalling galaxy or subcluster contributes minimally to the pressure. For the range of situations in the simulations that we have used, the assumption that $P_{\text{ram}} \gg P_{\text{grav}}$ and can therefore be omitted is never applicable, with $P_{\text{grav}} > P_{\text{ram}}$ at most times.

In addition, we emphasise that all stagnation point methods carry a significant uncertainty due to their sensitivity to the definition of the free stream variables. This is especially the case when including P_{grav} , and particularly near pericentre passage or in a disturbed ICM. In this analysis P_{grav} has been calculated according to a model for the stolen atmosphere that relies heavily on the free stream temperature and the gravitational potential (by a power of 2.5, see Eq. 2.7), which can improve velocity estimation significantly when the stagnation point method is valid. Considering the strong effect of the stolen atmosphere on the surrounding ICM, free stream variables measured too close to the galaxy or subcluster being analysed will be systematically enhanced over the free stream ICM, especially in the case of subsonic flow. We predict that this enhancement due to the stolen atmosphere, particularly the enhancement in temperature, will be visible during high resolution, deep observations — though projection effects may hide it well.

Because of significant observational uncertainties when defining the free stream values, using the new stagnation point method that includes compressibility and gravity will observationally provide more accurate values for velocity, though with greater uncertainties, rather than offering a method to provide precise and accurate velocity values. With further progress in both instrumentation and analysis of these methods, the new stagnation point method can be used as a stepping stone to providing accurate infall velocities of galaxies undergoing minor mergers.

6.2 Slingshot Tails

The slingshot tails illustrate another area of difficulty in understanding the situation within a merger. Not only are the flow patterns complex and well hidden by projection, but the orbit assumed from a galactic wake can be very misleading. This is especially the case if the merger isn't occurring within the plane of the sky. However, as both categories of slingshot tail, *overrun* and *arc-shaped*, develop through flow instabilities that occur around pericentre passage, they do signify a period of unstable flow. If the key characteristics can be spotted, this can definitively rule out the use of the stagnation point method.

6.3 Future Work

Further systematic testing of the stolen atmosphere effect on the stagnation point method within simulations is required to fully understand the applicability of our stagnation point method with compressibility and gravity under different conditions. This should be split up into several tests. First, several simulations with ideal stagnation point conditions (i.e. in a constant, linear flow) should be set up, each with a different velocity; the stagnation point method should then be applied with and without the gravitational modification to assess the applicability of this modification under unrealistically simple scenarios. There has been some interesting work regarding the effect of velocity on gravitational potentials by considering an empty potential in a steady flow (Ruderman & Spiegel, 1971) and dynamical friction (Thun et al., 2016; Bernal & Sánchez-Salcedo, 2013). Despite mostly focusing on the mass stripping and tail, this work may help in developing a stolen atmosphere model that better considers

how velocity will affect gravity's impact on the surrounding ICM of a galaxy. Secondly, the effect of the galaxy moving relative to another gravitational body should be tested to see whether, using realistic scales, the pull of a second body can significantly affect the pressure at the stagnation point before substantial flow disruptions occur. Other interesting gravitation related areas to study include: testing to find the conditions under which the cold core begins sloshing enough to significantly affect the gravitational potential at the upstream edge, the relaxation time of such sloshing under different conditions, and the effect of a second gravitational body on the internal structure of a galaxy if no sloshing is occurring. The effect of ICM gradients on the different stagnation point methods should also be considered, as determining some threshold would be useful when considering how to define stable flow within a real (i.e. complex) system.

A systematic study looking at the definition of the free stream variable values, and particularly at how to address the issues discussed in this thesis, would be a useful next step. One potential method that could yield reasonable results would be to model the ICM gradient, along with any significant (i.e. visible) ICM asymmetries, in order to better estimate what the ICM variables would be at the galaxy's location in the absence of the galaxy. However, this would be extremely complicated, and it would be difficult to quantify uncertainty in the results.

It would also be worthwhile to determine the cumulative uncertainties from the various factors that contribute to velocity uncertainty when calculated using the stagnation point methods listed in this thesis. In particular, the significant uncertainty in the estimation of galactic mass ([Vikhlinin et al., 2006](#); [Takizawa et al., 2010](#)) and additional uncertainty in the estimation of gravitational potential at a point on the upstream edge (particularly given the potential for cold core sloshing) could lead to huge uncertainties in the velocity estimate if gravity is included in the model.

One key factor to prove the validity of the stolen atmosphere effect, and therefore of the stagnation point method with gravity used here, is X-ray observation of the stolen atmosphere. For the stolen atmosphere to be visible, the surrounding ICM must be reasonably undisturbed, other than by the galaxy itself, and be at low enough redshift that the ICM surrounding the

galaxy has a reasonable signal-to-noise ratio and a large enough angular size that a gradient could be seen (especially considering projection issues). This makes NGC 1404 a fairly good candidate. However, this seems unlikely with today's telescopes, so finding the stolen atmosphere will rely on future missions, such as Athena may provide the data required.

7. Appendices

7.1 Defining The Stolen Atmosphere

The following derivation is taken from Roediger et al. (in prep.).

In order to calculate the pressure enhancement due to gravity, two drastic simplifications were made. Firstly, the galaxy/subcluster (galaxy hereon) will not move through its host cluster and, secondly, the galaxy will suddenly appear in a homogenous ICM. This allows us to consider the difference the gravitating body makes to the ICM without the system being affected by other sources of motion. We can call the variables of the initial homogenous medium ρ_{free} , T_{free} , and P_{free} , equivalent to the free stream variables of the stagnation point method. From this initial condition, we make three further assumptions:

- The ICM will settle into hydrostatic equilibrium (HSE):

$$\frac{\partial P}{\partial r} = -\rho g(r) \frac{\partial \Phi}{\partial r} \quad (7.1)$$

- The ICM functions as an ideal gas:

$$P = nk_B T = \frac{\rho}{m_p} k_B T \quad (7.2)$$

Where m_p is the average particle mass

- The settling is adiabatic, i.e. the entropy of the ICM remains constant:

$$S = \frac{k_B T}{n^{2/3}} = S_{\text{free}} \quad (7.3)$$

Therefore

$$n^{2/3} = \frac{k_B T}{S_{\text{free}}} \quad (7.4)$$

Next, we want to determine profiles as a function of the galaxy radius, r . We start by combining Equations 7.2 and 7.4:

$$\begin{aligned}
P &= \left(\frac{1}{S_{\text{free}}} \right) \cdot (k_B T)^{5/2} \\
\frac{\partial P}{\partial r} &= \left(\frac{1}{S_{\text{free}}} \right) \cdot \frac{\partial (k_B T)^{5/2}}{\partial r} \\
\frac{\partial P}{\partial r} &= \frac{-5}{2} \cdot \left(\frac{k_B T}{S_{\text{free}}} \right) \cdot \frac{\partial (k_B T)}{\partial r}
\end{aligned} \tag{7.5}$$

Then combining Equations 7.2 and 7.4 differently, we get:

$$\frac{\rho}{m_p} = \left(\frac{k_B T}{S_{\text{free}}} \right)^{3/2}$$

which can be substituted into into Equation 7.1:

$$\frac{\partial P}{\partial r} = \frac{-5m_p}{2} \cdot \left(\frac{k_B T}{S_{\text{free}}} \right)^{3/2} \cdot \frac{\partial \Phi}{\partial r} \tag{7.6}$$

Equations 7.5 and 7.6 can then be combined:

$$\left(\frac{k_B T}{S} \right)^{3/2} \frac{\partial (k_B T)}{\partial r} = \frac{5m_p}{2} \cdot \left(\frac{k_B T}{S_{\text{free}}} \right)^{3/2} \frac{\partial \Phi}{\partial r} \tag{7.7}$$

This can then be integrated from the boundary value of $k_B T_{\text{free}}$ at infinity, yielding:

$$k_B T(r) = k_B T_{\text{free}} - \frac{2}{5} m_p \cdot \Phi(r) \tag{7.8}$$

Thus we know that the ICM temperature increases towards the galaxy centre.

Next, we want to find the Pressure. We know $S = S_{\text{free}}$, so we can combine Equations 7.3 and 7.4 to get:

$$\begin{aligned}
n^{2/3} &= \frac{k_B T \cdot n_{\text{free}}^{2/3}}{k_B T_{\text{free}}} \\
n &= n_{\text{free}} \cdot \left(\frac{k_B T}{k_B T_{\text{free}}} \right)^{3/2}
\end{aligned} \tag{7.9}$$

If we use Equation 7.2 for a point at distance r from the galaxy's centre, we can substitute in Equation 7.9 to find:

$$P(r) = n(r) k_B T(r) = n_{\text{free}} \cdot \left(\frac{k_B T(r)}{k_B T_{\text{free}}} \right)^{2/3} \cdot k_B T(r)$$

$$P(r) = n_{\text{free}} \cdot \left(\frac{k_B T(r)}{k_B T_{\text{free}}} \right)^{3/2} \cdot k_B T(r)$$

$$P(r) = P_{\text{free}} \cdot \left(\frac{k_B T(r)}{k_B T_{\text{free}}} \right)^{3/2} \cdot \frac{k_B T(r)}{k_B T_{\text{free}}}$$

$$P(r) = P_{\text{free}} \cdot \left(\frac{k_B T(r)}{k_B T_{\text{free}}} \right)^{5/2} \quad (7.10)$$

The variables at r can be split into the background value and the gravitational enhancement, e.g. $P(r) = P_{\text{grav}}(r) + P_{\text{free}}$:

$$P_{\text{grav}}(r) = P_{\text{free}} \times \left[\left(\frac{k_B T(r)}{k_B T_{\text{free}}} \right)^{5/2} - 1 \right] \quad (7.11)$$

which can be combined with Equation 7.8 to get:

$$\frac{P_{\text{grav}}(r)}{P_{\text{free}}} = \left(\frac{k_B T_{\text{free}} - \frac{2}{5} m_p \cdot \Phi(r)}{k_B T_{\text{free}}} \right)^{5/2} - 1 \quad (7.12)$$

Equation 7.12 is equivalent to Equation 2.7 in the main text.

Bibliography

- Abell G. O., Corwin, Harold G. J., Olowin R. P., 1989, [The Astrophysical Journal Supplement Series](#), 70, 1
- Acreman D. M., Stevens I. R., Ponman T. J., Sakelliou I., 2003, [Monthly Notice of the Royal Astronomical Society](#), 341, 1333
- Ascasibar Y., Markevitch M., 2006, [The Astrophysical Journal](#), 650, 102
- Avila-Reese V., Firmani C., Klypin A., Kravtsov A. V., 1999, [Monthly Notices of the Royal Astronomical Society](#), 310, 527
- Batchelor G. K., 2017, 8. Introduction to Fluid Dynamics, 1 edn. Cambridge University Press, Cambridge, [doi:10.1515/9781400883073-010](#)
- Bernal C. G., Sánchez-Salcedo F. J., 2013, [The Astrophysical Journal](#), 775, 72
- Biermann P., Kronberg P. P., 1983, [The Astrophysical Journal](#), 268, L69
- Böhringer H., Briel U. G., Schwarz R. A., Voges W., Hartner G., Trümper J., 1994, [Nature](#), 368, 828
- Bonafede A., Govoni F., Feretti L., Murgia M., Giovannini G., Brüggén M., 2011, [Astronomy & Astrophysics](#), 530, A24
- Cavaliere A. G., Gursky H., Tucker W. H., 1971, [Nature](#), 231, 437
- Cen R., Pop A. R., Bahcall N. A., 2014, [Proceedings of the National Academy of Sciences of the United States of America](#), 111, 7914
- Clowe D., Bradač M., Gonzalez A. H., Markevitch M., Randall S. W., Jones C., Zaritsky D., 2006, [The Astrophysical Journal](#), 648, L109
- De Grandi S., et al., 2016, [Astronomy & Astrophysics](#), 592, A154
- Eckert D., et al., 2017, [Astronomy & Astrophysics](#), 605, A25
- Eisenstein D. J., Hut P., 1997, [The Astrophysical Journal](#), 498, 137
- Fabian A. C., 1994, [Annual Review of Astronomy and Astrophysics](#), 32, 277

- Fabian A. C., 2002, in Gilfanov M., Sunyaev R., Churazov E., eds, , *Lighthouses of the Universe: The Most Luminous Celestial Objects and Their Use for Cosmology*. Springer, Berlin/Heidelberg, pp 24–36, [doi:10.1007/10856495_3](https://doi.org/10.1007/10856495_3)
- Farrar G. R., Rosen R. A., 2007, *Physical Review Letters*, 98, 171302
- Forman W., Kellogg E., Gursky H., Tananbaum H., Giacconi R., 1972, *The Astrophysical Journal*, 178, 309
- Fryxell B., et al., 2000, *The Astrophysical Journal Supplement Series*, 131, 273
- Giovannini G., Bonafede A., Feretti L., Govoni F., Murgia M., Ferrari F., Monti G., 2009, *Astronomy & Astrophysics*, 507, 1257
- Godwin J. G., Metcalfe N., Peach J. V., 1983, *Monthly Notices of the Royal Astronomical Society*, 202, 113
- Gott J. R. I., Rees M. J., 1975, *Astronomy & Astrophysics*, 45, 365
- Gu L., et al., 2019, *Nature Astronomy*, 3, 838
- Gunn J. E., Gott, J. Richard I., 1972, *The Astrophysical Journal*, 176, 1
- Hernquist L., Lars 1990, *The Astrophysical Journal*, 356, 359
- Ichinohe Y., Werner N., Simionescu A., Allen S. W., Canning R. E. A., Ehlert S., Mernier F., Takahashi T., 2015, *Monthly Notices of the Royal Astronomical Society*, 448, 2971
- Jang-Condell H., Hernquist L., 2001, *The Astrophysical Journal*, 548, 68
- Jarosik N., et al., 2011, *The Astrophysical Journal Supplement Series*, 192, 14
- Jones C., Mandel E., Schwarz J., Forman W., Murray S. S., Harnden, F. R. J., 1979, *The Astrophysical Journal*, 234, L21
- Jones C., Stern C., Forman W., Breen J., David L., Tucker W., Franx M., 1997, *The Astrophysical Journal*, 482, 143
- Kaastra J. S., Paerels F. B., Durret F., Schindler S., Richter P., 2008, *Space Science Reviews*, 134, 155
- Kahn F. D., Waltjer L., 1959, *The Astrophysical Journal*, 130, 705
- Kraft R. P., et al., 2017, *The Astrophysical Journal*, 848, 27
- Kravtsov A. V., Borgani S., 2012, *Annual Review of Astronomy and Astrophysics*, 50, 353
- Lifshitz E. M., Landau L. D., 1959, *Fluid Mechanics*. Pergamon Press Ltd., Oxford

- Machacek M., Dosaj A., Forman W., Jones C., Markevitch M., Vikhlinin A., Warmflash A., Kraft R., 2005a, [The Astrophysical Journal](#), 621, 663
- Machacek M., Jones C., Forman W. R., Nulsen P. E. J., 2005b, [The Astrophysical Journal](#), 644, 155
- Markevitch M., Vikhlinin A., 2007, [Physics Reports](#), 443, 1
- Markevitch M., Sarazin C. L., Vikhlinin A., 1999, [The Astrophysical Journal](#), 521, 526
- Markevitch M., et al., 2000, [The Astrophysical Journal](#), 541, 542
- Markevitch M., Gonzalez A. H., David L., Vikhlinin A., Murray S., Forman W., Jones C., Tucker W., 2002, [The Astrophysical Journal](#), 567, L27
- Markevitch M., Govoni F., Brunetti G., Jerius D., 2005, [The Astrophysical Journal](#), 627, 733
- Milosavljević M., Koda J., Nagai D., Nakar E., Shapiro P. R., 2007, [The Astrophysical Journal](#), 661, L131
- Morandi A., Sun M., Forman W., Jones C., 2015, [Monthly Notices of the Royal Astronomical Society](#), 450, 2261
- Mori M., Burkert A., 2000, [The Astrophysical Journal](#), 538, 559
- Navarro J. F., Frenk C. S., White S. D. M., 1995, [Monthly Notices of the Royal Astronomical Society](#), 275, 56
- Navarro J. F., Frenk C. S., White S. D. M., 1997, [The Astrophysical Journal](#), 490, 493
- Neill J. D., Seibert M., Tully R. B., Courtois H., Sorce J. G., Jarrett T. H., Scowcroft V., Masci F. J., 2014, [Astrophysical Journal](#), 792
- Nozawa S., Itoh N., Kohyama Y., 1998, [The Astrophysical Journal](#), Volume 507, Issue 2, pp. 530-557., 507, 530
- Nulsen P. E. J., 1982, [Monthly Notices of the Royal Astronomical Society](#), 198, 1007
- Pizzella A., Corsini E. M., Dalla Bonta E., Sarzi M., Coccatto L., Bertola F., 2005, [The Astrophysical Journal](#), 631, 785
- Poole G. B., Fardal M. A., Babul A., McCarthy I. G., Quinn T., Wadsley J., 2006, [Monthly Notices of the Royal Astronomical Society](#), 373, 881
- Prasad D., Sharma P., Babul A., 2018, [The Astrophysical Journal](#), 863, 62
- Pratt G. W., Croston J. H., Arnaud M., Böhringer H., 2009, [Astronomy and Astrophysics](#), 498, 361
- Primack J. R., 2009, [AIP Conference Proceedings](#), pp 101–137

- Rasia E., Mazzotta P., Borgani S., Moscardini L., Dolag K., Tormen G., Diaferio A., Murante G., 2005, [The Astrophysical Journal](#), 618, L1
- Ricker P. M., 1998, [The Astrophysical Journal](#), 496, 670
- Ricker P. M., Sarazin C. L., 2001, [The Astrophysical Journal](#), 561, 621
- Roediger E., Brüggén M., 2006, [Monthly Notices of the Royal Astronomical Society](#), 369, 567
- Roediger E., et al., 2012, [Monthly Notices of the Royal Astronomical Society](#), 420, 3632
- Roediger E., et al., 2015a, [Astrophysical Journal](#), 806, 103
- Roediger E., et al., 2015b, [Astrophysical Journal](#), 806, 104
- Rubin V. C., Thonnard N., Ford, W. K. J., 1980, [The Astrophysical Journal](#), 238, 471
- Ruderman M. A., Spiegel E. A., 1971, [The Astrophysical Journal](#), 165, 1
- Sadat R., 1997, in Valls-Gabaud D., Hendry M., Molaro P., Chamcham K., eds, *Astronomical Society of the Pacific Conference Series Vol. 126, From Quantum Fluctuations to Cosmological Structures*. p. 349 ([arXiv:astro-ph/9702050](#))
- Sarazin C. L., 1986, [Reviews of Modern Physics](#), 58, 1
- Sarazin C. L., 2008, in Plionis M., Hughes D., López-Cruz O., eds, , Vol. 740, *Lecture Notes in Physics: A Pan-Chromatic View of Clusters of Galaxies and the Large-Scale Structure*. Springer Netherlands, Dordrecht, pp 1–30, [doi:10.1007/978-1-4020-6941-3_1](#)
- Scharf C. A., Zurek D. R., Bureau M., 2005, [The Astrophysical Journal](#), 633, 154
- Schneider P., 2006, *Extragalactic Astronomy and Cosmology*. Springer Berlin Heidelberg, Berlin, Heidelberg, [doi:10.1007/978-3-540-33175-9](#)
- Sheardown A., et al., 2018, [The Astrophysical Journal](#), 865, 118
- Sheardown A., et al., 2019, [The Astrophysical Journal](#), 874, 112
- Shi X., Komatsu E., Nagai D., Lau E. T., 2016, [Monthly Notices of the Royal Astronomical Society](#), 455, 2936
- Springel V., Farrar G. R., 2007, [Monthly Notices of the Royal Astronomical Society](#), 380, 911
- Steinhauser D., Schindler S., Springel V., 2016, [Astronomy & Astrophysics](#), 591, A51
- Su Y., Irwin J. A., White R. E., Cooper M. C., 2015, [Astrophysical Journal](#), 806, 156

- Su Y., et al., 2017a, [The Astrophysical Journal](#), 834, 74
- Su Y., et al., 2017b, [The Astrophysical Journal](#), 835, 19
- Su Y., et al., 2017c, [The Astrophysical Journal](#), 851, 69
- Su Y., et al., 2019, [Bulletin of the American Astronomical Society](#), 51, 476
- Takizawa M., Nagino R., Matsushita K., 2010, [Publications of the Astronomical Society of Japan](#), 62, 951
- Thun D., Kuiper R., Schmidt F., Kley W., 2016, [Astronomy & Astrophysics](#), 589, A10
- Tielens A. G., 2005, [The physics and chemistry of the interstellar medium](#). Cambridge University Press, [doi:10.1017/CBO9780511819056](https://doi.org/10.1017/CBO9780511819056), [/core/books/physics-and-chemistry-of-the-interstellar-medium/B71008A57D96A2875E851DAEA70B16AE](#)
- Tonnesen S., Stone J., 2014, [The Astrophysical Journal](#), 795, 148
- Turk M. J., Smith B. D., Oishi J. S., Skory S., Skillman S. W., Abel T., Norman M. L., 2011, [The Astrophysical Journal Supplement Series](#), 192, 9
- Van Dyke M., 1982, [An Album of Fluid Motion](#). The Parabolic Press, Stanford
- Vijayaraghavan R., Ricker P. M., 2015, [Monthly Notices of the Royal Astronomical Society](#), 449, 2312
- Vikhlinin A., 2006, [The Astrophysical Journal](#), 640, 710
- Vikhlinin A. A., Markevitch M. L., 2002, [Astronomy Letters](#), 28, 495
- Vikhlinin A., Markevitch M., Murray S. S., 2001, [The Astrophysical Journal](#), 551, 160
- Vikhlinin A., Kravtsov A., Forman W., Jones C., Markevitch M., Murray S. S., Van Speybroeck L., 2006, [The Astrophysical Journal](#), 640, 691
- Vink J., Jacco 2008, [Astronomy & Astrophysics](#), 486, 837
- Zhang C., Churazov E., Forman W. R., Jones C., 2019, [Monthly Notices of the Royal Astronomical Society](#), 482, 20
- ZuHone J., Markevitch M., 2009, in [AIP Conference Proceedings](#). American Institute of Physics, pp 383–386 ([arXiv:0909.0560](https://arxiv.org/abs/0909.0560)), [doi:10.1063/1.3293082](https://doi.org/10.1063/1.3293082), <http://aip.scitation.org/doi/abs/10.1063/1.3293082>
- ZuHone J. A., Roediger E., 2016, [Journal of Plasma Physics](#), 82

Zuhone J. A., 2011, [Astrophysical Journal](#), 728, 54

Zwicky F., 1933, *Helvetica Physica Acta*, 6, 110

Zwicky F., 1937, [The Astrophysical Journal](#), 86, 217